GROWTH AND INTERACTION OF GOLD ON THE FACETED RHENIUM $(12\bar{3}1)$ SURFACE

BY ROBERT CHRISTOPH WOLFGANG BAIER

A thesis submitted to the

Graduate School—New Brunswick

Rutgers, The State University of New Jersey

in partial fulfillment of the requirements

for the degree of

Master of Science

Graduate Program in Physics

Written under the direction of

Professor Dr. Theodore E. Madey

and approved by

_____

_____

_____

New Brunswick, New Jersey

October, 2008

ABSTRACT OF THE THESIS

Growth and interaction of gold on the faceted rhenium $(12\bar{3}1)$ surface

by Robert Christoph Wolfgang Baier

Thesis Director: Professor Dr. Theodore E. Madey

Heterogeneous catalysts are a field of major interest is in surface science. The development of new supported model catalysts with a narrow size distribution is a central aspect of this research. One possibility to create narrow size distributions is the use of faceted surface structures as self assembled templates on which to grow metal nanoclusters. In this thesis, a faceted rhenium single crystal is used as a template for gold growth; the facets were induced by oxygen. The orientation of the planar rhenium crystal is $(12\bar{3}1)$, whereby the facets consist of two sided ridges with $(11\bar{2}1)$ and $(01\bar{1}0)$ orientations. The way of growth and the influence of gold on the faceted rhenium crystal is studied by means of Auger electron spectroscopy (AES), low energy electron diffraction (LEED) and scanning tunneling microscopy (STM). Also, the influence of gold on a planar Re $(12\bar{3}1)$ surface is studied.

It was found that gold grows in Volmer-Weber growth mode on the faceted rhenium substrate. For coverages of 0.4 ML and 0.8 ML gold formed 2D islands on top of the ridges, whereby for 1.4 ML coverage 3D islands were observed. Annealing of the

gold covered surface structure led to drastic changes in the surfaces morphology. After the first annealing to a temperature of approximately 870 K for approximately 30 minutes gold atoms wet the rhenium template. Further annealing of the surface led to the development of a three sided pyramidal structure; the orientation of the pyramids still contains the orientation of the original two sided ridges. Continued annealing to temperatures of approximately 970 K developed a totally new surface structure. Two sided ridges were found again on the surface, but with a different orientation and shape than the original template structure. Finally, after annealing above 1200 K, all surface structures were destroyed and gold was desorbed from the surface. The morphological change is attributed to gold induced faceting on the oxygen induced surface structure.

The pyramid structure was examined more detailed. Thereby a coverage dependency in the development of the facets was found. For 0.4 ML one of the pyramids sides is underdeveloped. For 0.8 ML and 1.4 ML all sides of the pyramids structure were fully developed; small destruction of the pyramids for 1.4 ML coverage is attributed to beginning destruction of the original oxygen induced ridges. The orientations of the pyramids facets were determined as $(01\bar{1}0)$, $(11\bar{2}0)$ and $(12\bar{3}2)$. Analysis of the facets atomic structure led to the suspicion, that the $(12\bar{3}2)$ facet is covered with a gold overlayer whereas the $(01\bar{1}0)$ facet is not covered with gold.

Also the influence of gold on planar Re $(12\bar{3}1)$ was examined. After annealing of the gold covered planar crystal (Coverage: 0.8 ML) two sided ridges were found on the surface. The orientation of this ridges was rotated by around 90 ° with respect to the oxygen induced ridges. It is believed that gold has the ability to induce faceting on the planar Re $(12\bar{3}1)$ surface.

Keywords: adsorbate-induced faceting, oxygen-induced faceting, gold-induced faceting, rhenium, gold, oxygen, two sided ridges, three-sided pyramids

Acknowledgements

It was a big honor for me to be part of Ted Madey's group. Ted was a great mentor, who combined deep scientific knowledge with a great warm hearted character in a unique way. I also want to thank Govind for all his support during the time we spent together. His advices and the many discussions we had helped me a lot. In addition, I had the best cups of tea during my time at Rutgers in his apartment. Finally I want to thank Professor Bob Bartynski for helping me to finish this work.

IN MEMORIAM

Professor

Theodore E. Madey

(1937 - 2008)

Table of Contents

Abstract ii

Acknowledgements iv

List of Figures viii

1. Introduction 1

2. Materials 5

2.1. Rhenium 5

2.2. Gold 6

3. Nucleation and growth of thin films 9

4. Adsorbate induced faceting 16

5. Experimental techniques 20

5.1. Ultra high vacuum (UHV) 21

5.2. Low energy electron diffraction (LEED) 24

5.3. Auger electron spectroscopy (AES) 29

5.4. Scanning tunneling microscopy (STM) 33

6. Experimental results 38

6.1. Gold deposition on a faceted Re $(12\bar{3}1)$ surface 42

6.1.1. Oxygen induced ridges on Re $(12\bar{3}1)$ 42

6.1.2. Gold nanoclusters on the faceted Re surface 45

6.1.3. Temperature dependence of the morphological change 49
6.1.4. Coverage dependence of the morphological change 54
6.1.5. Gold induced three sided pyramids 58
6.1.6. Controlling the size of the pyramids 66
6.2. Gold induced faceting on a planar Re $(12\bar{3}1)$ substrate 69

7. Conclusion 74

Appendix A. Preparation of tungsten tips for STM 79

Appendix B. List of abbreviations and acronyms 81

References 82

Vita 85

List of Figures

1.1. Development of the world population 1

2.1. Rhenium crystal 6

2.2. The mask of Agamemnon 7

3.1. The three primary modes of thin film growth 9

3.2. Comparison: FM/VW growth-mode 10

3.3. Ehrlich-Schwoebel-Barrier 14

4.1. Schematic of adsorbate-induced faceting 16

4.2. Re(12$\bar{3}$1) surface structure 18

4.3. Morphological evolution of facets on Re(12$\bar{3}$1) 19

5.1. UHV-chamber 21

5.2. Different vacuum pumps 22

5.3. LEED schematics 24

5.4. Electron mean free path in metals 26

5.5. Bragg-Conditions 27

5.6. Identification of surface structures by LEED 28

5.7. Auger effect 29

5.8. AES: Characteristic peaks 31

5.9. AES: Identification of different growth modes 32

5.10. Electron tunneling; principle of STM 34

5.11. Schematic of a STM 36

5.12. STM: Different modes of scanning 37

6.1. STM image; 500 nm × 500 nm; two sided ridges on Re (12$\bar{3}$1) 42
6.2. Line scan of two sided ridges 43
6.3. Details of the sawtooth ridges 44
6.4. LEED image of two sided ridges 45
6.5. STM images; 50 nm × 50 nm; gold clusters 46
6.6. AES ratio Au/Re 47
6.7. STM image; 50 nm × 50 nm; Determination of gold coverage 48
6.8. STM image; 50 nm × 50 nm; gold nanoclusters 50
6.9. STM image; 50 nm × 50 nm; gold wets surface 51
6.10. STM image; 50 nm × 50 nm; three sided pyramids 52
6.11. STM image; 50 nm × 50 nm; two sided ridges 53
6.12. STM images; 50 nm × 50 nm; coverage dependency 56
6.13. Details about the pyramids structure 59
6.14. LEED image of the pyramid structure 61
6.15. STM image; 25 nm × 25 nm; all pyramidal facets 63
6.16. Atomic structure of the first facet 64
6.17. Atomic structure of the second facet 65
6.18. Correlation of the pyramid size 67
6.19. STM image; 50 nm × 50 nm; gold induced two sided ridges 69
6.20. Line scan of gold induced facet 70
6.21. Comparison Au/O induced ridges 70
6.22. Stereographic projection of hcp lattice 71
6.23. Comparison: gold induced facets 72
A.1. Homemade STM tips 80

Chapter 1

Introduction

The world population keeps growing and growing. By now, more than 6 billion people live on earth (Figure: 1.1) [1]. Also the two most populated countries, China and India, are undergoing a drastic evolution from developing countries to industrial nations right now. One of the major problems that emerges with fast growing population and technological evolution is environmental pollution. More and more people start using modern technologies, like electricity and automobiles, which comes along with higher emission of poisonous substances. A good example of this problems can be observed right now in Beijing, where the 2008 Summer Olympic Games take place. In spite of large efforts by the Chinese government it was not possible to hide the increasing level of environmental pollution there [2].

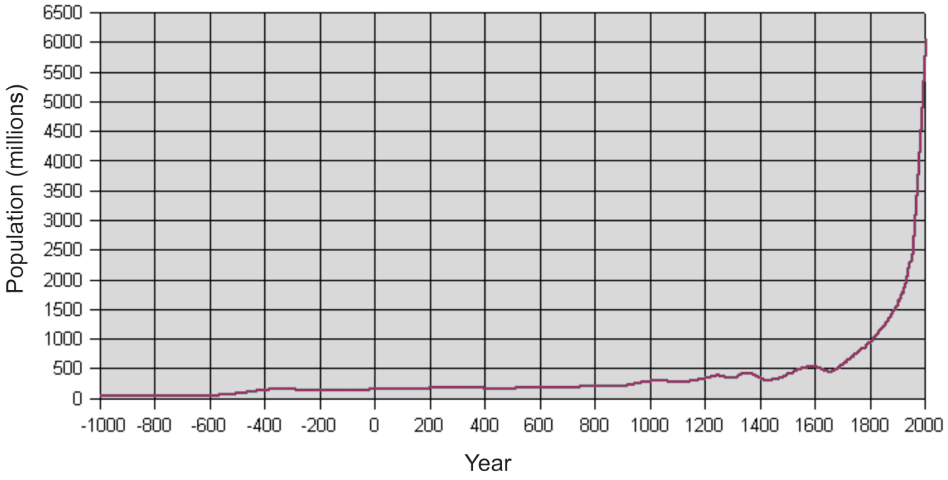

Figure 1.1: Development of the world population

In order to limit environmental pollution, the development of new, cleaner technologies is essential. One key to achieve this goal are modern catalysts. By making chemical reactions more efficient and selective it is possible to reduce the level of emission drastically. In 1835 Jöns Jakob Berzelius realized first that a multitude of chemical reactions can only occur in the presence of certain substances. These substances, which unlike a chemical reagent are not consumed by the reaction, are called catalysts. Within the last 173 years catalysts developed to a major technology for many applications. It is difficult to imagine today's world without modern catalysts. They are almost everywhere; oil refineries use them to produce gasoline, modern cars became more environmental friendly through them and, just as a side note, even our body would not function without enzymes that act as bio-catalysts.

A very common type of catalyst found in technology are heterogeneous catalysts. Heterogeneous means that the the catalyst is in a different phase than the reactants. The major challenges of modern heterogeneous catalysis research is to optimize chemical reactions; that means to obtain higher reaction rates and selectivities for chemical processes [3]. For a long time the main method of optimizing this processes was simply trial and error. Even if you knew about the broad features of the catalysts, it was not possible to study the catalytic reaction itself. This was due to the complexity of these catalysts, but it was also due to the lack of characterization of them. Real heterogeneous catalysts consist of metal nanoparticles, which are spread on a porous substrate; they provide a surface on which chemical reactions can take place. It is hard to obtain information about the structure of this surfaces and the morphology of the particles, since the number of methods to study them is limited; only broad information about the particles size distribution could be obtained by electron microscopy. Therefore, model catalysts were developed. Model catalysts are based on well ordered extended surfaces of catalytic metals prepared under ultra high vacuum (UHV) conditions. The main advantage of

these model catalysts is the possibility of using the variety of UHV-characterization techniques to explore them. Hence, the atomic structure and electrical properties of these catalysts became accessible and it became possible to characterize them completely. But still there was a problem. The model catalysts could not account for two important features of real catalysts; the finite cluster size and the supporting porous substrate. In order to close this so called "material gap" a new type of model catalysts, the supported model catalysts, was developed. Supported model catalysts are small metal particles supported on a planar surface. They can be fabricated by nucleation and growth of metal clusters on supporting surfaces under UHV conditions. However, there is still one big difference between supported model catalysts and real catalysts. Real catalytic reactions take place at atmospheric pressure or even high pressure, while supported model catalysts are studied in UHV. To overcome this "pressure-gap", high-pressure cells inside the UHV system are used. So, the catalytic reaction can take place in high-pressure atmosphere, whereas the techniques of UHV can still be used to analyze the catalyst before and after the reaction. [4], [5]

For the next generation of heterogeneous catalysts, geometrical and electrical properties of the metal nanoparticles play a major role [3]. A proper control over these parameters might lead to a new generation of highly selective and reactive catalysts.
One possible approach to obtain supported model catalysts with narrow size distribution is to use faceted surfaces as self-assembled nanotemplates on which to grow nanoclusters. Nanoclusters may grow preferentially on certain sides of the facets and thereby develop the desired narrow size distribution.

Within this work the interaction between gold atoms and a faceted rhenium substrate is studied. Two sided ridges were created on a planar Re $(12\bar{3}1)$ surface by oxygen-induction, afterwards gold atoms were dosed on the surface. Both metals, gold and rhenium, are very popular in modern catalysts. A platinum-rhenium catalyst is used

to produce lead-free gasoline, for example [6]. Gold, one the other hand, becomes very reactive in the nanometer size regime, for which reason it is one of the most popular metals in catalysis [7]. So, rhenium and gold is a very interesting combination, that might lead to future applications in catalysis. The goal of this work is to gain understanding about the gold/rhenium system. Hence the growth mode of gold atoms on the faceted rhenium surface, the influence of annealing the gold/rhenium system and many other interesting topics were studied. Thereby surprising results were obtained and new physical properties discovered.

Chapter 2

Materials

2.1 Rhenium

Rhenium is the chemical element with the symbol Re and the atomic number 75. It crystallizes in the hexagonal close-packed structure (hcp) with unit cell parameters a = 2.761 Å and c = 4.458 Å [8]. It was discovered first in 1925 by the german chemists Walter Noddack, Ida Tacke and Walter Berg, that named it rhenium in honor of their rhenish homeland (Latain: Rhenus = Rhine). It is a silverly white, lustrous metal with a very high density of 21.02 $\frac{g}{cm^3}$. This density is exceeded only by the density of platinum, iridium and osmium. It has a melting point of 3459 K, which is only exceeded by the elements of tungsten and carbon, and a boiling point of 5869 K, the highest of any metal. Below 1.7 K rhenium becomes superconducting.

Rhenium is, together with rhodium, ruthenium and osmium, one of the rarest non-decaying elements on earth with an abundance of approximately 1 part per billion. It neither occurs in elemental form in free nature, nor as a compound in a distinct mineral species. Most of the rhenium which is used today was extracted from some molybdenum-ores, which can contain up to 0.02% rhenium. [6]

The major application of rhenium is in high-temperature technique, due to its high melting point. Rhenium is used in high-temperature resistant nickel-superalloys, which are used to built jet-engine parts, for example [9]. But it is also very important for catalyst applications, which is more related to this work. A platinum-rhenium catalyst is used in the oil-industry to produce lead-free high octane gasoline in a process called

"chemical Reforming". The advantage of the platinum-rhenium catalyst is its very high resistance to poisoning from sulfur, nitrogen and phosphorus. [6]

Figure 2.1: A rhenium crystal [10].

2.2 Gold

Gold is the chemical element with the symbol Au (Latain: Aurum = Gold) and the atomic number 79. It crystallizes in the cubic face centered structure, the unit cell parameter is 4.078 Å [11]. It is a yellow colored precious metal, chemically belonging to the noble metals. With a density of 19.32 $\frac{g}{cm^3}$ it is a very dense metal. Its melting point is 1337 K and its boiling point is 3129 K ; both values are relatively low compared to other metals. Gold is a very good conductor for heat and electricity with a thermal conductivity of 318 $\frac{W}{K \cdot m}$ (at 300 K) and an electrical conductivity of 45.2 $\cdot 10^6$ $\frac{1}{\Omega \cdot m}$. It is the most malleable and ductile of all metals; one ounce of gold can be beaten out to 300 ft^2. [12]

Gold is known and highly valued from earliest times. People were always fascinated by its "golden" color; it also was easy to work with due to its physical properties. The special rank of gold is even expressed in the Bible. When the three Magi visited the

newborn Jesus Christ, they gave him three gifts: frankincense, myrrh and gold [13]. And gold did not loose a bit of its appraisal nowadays. Just some month ago, the gold price reached a new all-time high [14].

Figure 2.2: The Mask of Agamemnon ; a golden funeral mask, discovered at Mycenae in 1876 by Heinrich Schliemann. The mask is dated around 1550-1500 B.C. It shows the special rank that gold had from earliest times on.[15]

Gold has a broad range of applications. It is one of the most popular funds, be it gold bars or gold coins. Also it still is of the most favored and expensive metals for jewelery. But it is very important for technical applications, too. Its physical and chemical properties, like the good conductibility or its inertance against chemical processes like corrosion and oxidation, make it very interesting for a manifold of applications including as a coating material for electronic connections or in medical devices.

Interestingly it is exactly this inertness of gold that should normally make it useless for applications in heterogeneous catalysts, where a high chemical activity is required. But still it is one of the major metals in catalysts. This is based on another exciting

property of gold. It was found that gold changes its character drastically in the nanometer size regime. At particle-sizes around 5 nm highly dispersed gold particles become very reactive. So, gold nanoclusters play an important role in catalytic reactions like CO-Oxidation [16], [7], [17].

Chapter 3

Nucleation and growth of thin films

When thin films are grown on metal surfaces one question that occurs is the way in which these metal films grow onto the substrates. In general, the growth mode depends on a variety of variables like the substrate's crystallinity and cleanliness, the films material and the flux and thermodynamical energy of the incident particles. Nevertheless, there are three different fundamental growth modes to distinguish, each of them named after the discovering scientist (Figure: 3.1).

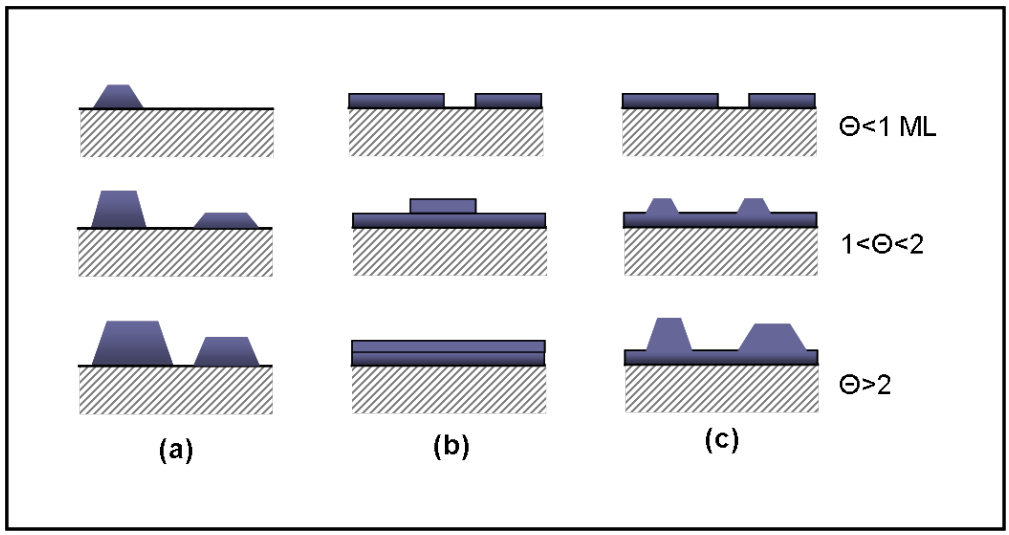

Figure 3.1: Cross-section views of the three primary modes of thin film growth including (a) Volmer-Weber (VW: island formation), (b) Frank-van der Merwe (FM: layer-by-layer), and (c) Stranski-Krastanov (SK: layer-plus-island). Each mode is shown for several different amounts of surface coverage θ

Volmer-Weber (VW) growth: In this growth mode the adatoms start building clusters right from the beginning. They build islands on top of the substrate layer, which are separated by uncovered substrate surface areas. Therefore this mode is also known as island growth.

Frank-van der Merwe (FM) growth: In this growth mode, which is often also called layer-by layer-growth, the deposited metals wet a single atomic layer completely before they start to wet a new layer. Therefore the metals on the surface grow layer by layer.

Stranski-Krastanov (SK) growth: In this growth mode the atoms wet the first substrate layers completely. However, when a critical layer thickness is reached, the growth mode switches from layer by layer growth to island growth. Thereby the critical layer thickness depends on the physical and chemical properties of the system, especially on the lattice misfit between film and substrates lattice constant.

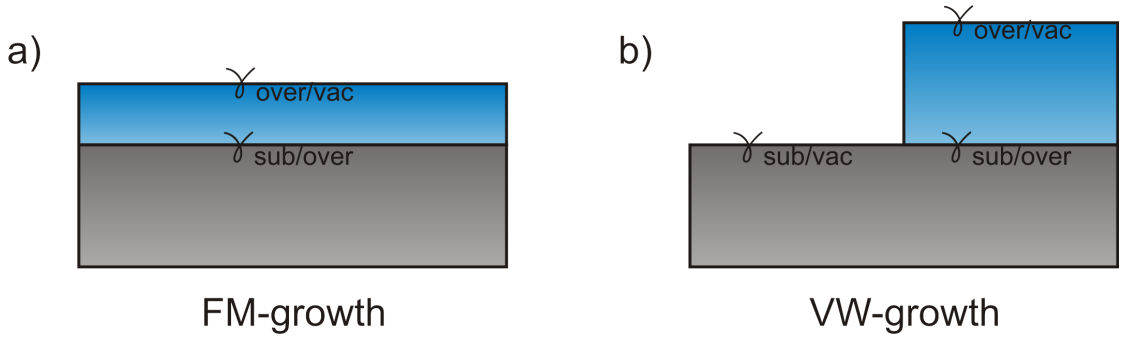

Figure 3.2: Comparison between Frank-van der Merwe growth and Volmer-Weber growth

Many parameters influence the way of growth, so that it is not possible to make precise predictions about it. But it is possible to get a rough estimation about which of the three growth modes will occur most likely just by energetic considerations. If you compare Volmer-Weber and Frank-van der Merwe growth, there are three different interfaces for the systems; substrate-vacuum, substrate-overlayer and overlayer-vacuum (Figure: 3.2). All of the interfaces have different surface free energies per unit area ($\gamma_{i/j}$).

Considering only these surface free energies it is possible to make some energetic argument about which growth mode is most likely. Therefore we calculate the difference in surface free energy between both of the growth modes; in order to obtain a quantitative result, it is assumed that islands occupy half the available surface area (A) for Volmer-Weber growth [18].

$$\begin{aligned} \Delta E &= E_{FV} - E_{VW} \\ &= \left(\gamma_{over/vac} + \gamma_{sub/over}\right) \cdot A - \frac{1}{2}\left(\gamma_{over/vac} + \gamma_{sub/over} + \gamma_{sub/vac}\right) \cdot A \end{aligned} \quad (3.1)$$

From this result it is possible to get conditions for the three different growth modes:

$$\text{Frank-van der Merwe growth: } \gamma_{sub/vac} > \gamma_{over/vac} + \gamma_{sub/over} \quad (3.2)$$

$$\text{Volmer-Weber growth: } \gamma_{sub/vac} < \gamma_{over/vac} + \gamma_{sub/over} \quad (3.3)$$

$$\text{Stranski-Krastanov growth: } \gamma_{sub/vac} \cong \gamma_{over/vac} + \gamma_{sub/over} \quad (3.4)$$

There we also consider that Stranski-Krastanov growth is a mixture of both of the other growth modes. So Stranski-Krastanov growth should appear in the transition area between Volmer-Weber and Frank-van der Merwe growth.

This results can be used to make some rough predictions about which growth mode is to expect for certain substrate/overlayer combinations. So, for example, is the surface free energy for transition metals usually larger than or at least comparable to that of oxides[1]. This means that the metal/oxide interfacial surface free energy must be very small for wetting of metal atoms on oxide surfaces to occur . It was shown experimentally that the interfacial surface free energy is never that small. So, it is very unlikely for transition metals to wet an oxide surface. This is consistent with the usual observation that transition metal catalysts form 3D particles on silica or alumina support.[19]

[1]Examples given: γ_W= 2900 erg/cm^2, γ_{MgO}= 1200 erg/cm^2 ; 1 erg= 1.0×10^{-7} Joule

The process that leads to the different growth modes is called nucleation. Adatoms that are dosed on a surface diffuse on it. They collide with other adatoms and built metastable clusters after a collision. These clusters, called nuclei, become stable when a critical number of diffusing atoms collides. As the surface starts to fill with stable nuclei, these clusters can unite to bigger cluster, finally covering the surface in one of the three growth modes. In general, nucleation is divided into two categories: Homogeneous and heterogeneous nucleation.

For homogeneous nucleation the surface is assumed to be defect free. So, the atoms diffuse and collide randomly on the surface. After several collisions they build stable clusters at various sites on the surface. The clusters become stable when a critical cluster size is reached. The critical cluster size depends on the total free energy of a cluster and can be determined by the following equation [20]:

$$r_{crit.} = \frac{2 \cdot \Omega \cdot \gamma_n}{k \cdot T_s \cdot ln(\zeta)} \tag{3.5}$$

where:
Ω = Atomic volume
γ_n = Surface free energy of nucleus
k = Boltzmann constant
T_s = Substrates temperature
ζ = Degree of supersaturaion

For many systems the critical cluster size turns out to be only one or two atoms.

With an increasing number of adatoms on the surface the number of stable nuclei also increases. At some point it becomes more likely for adatoms to diffuse to an existing cluster than to collide with other adatoms to built a new cluster. This state is characterized by a saturation in the number of clusters on the surface. Adopting a model with

slow adatom desorption, which means that we ignore desorption of isolated adatoms from the surface, and a critical cluster size of one, so that a dimer, once formed, will not dissociate, we can calculate the saturation density N of nuclei on the surface. Thereby we assume an average separation distance for for gold clusters, so we can get a rate for adatom incorporation into existing clusters. It is also possible to get a rate for buildup of adatoms from the vapor. Neglecting creation of new nuclei, which is true at saturation, we can use a steady state approximation and assume that both rates are equal. Solving this, we finally get for the nuclei saturation density N [19]:

$$N = \left(\frac{40 \cdot F}{a^2 \cdot \upsilon \cdot exp(-\frac{E_{Diff}}{R \cdot T})} \right)^{\frac{1}{2}} \tag{3.6}$$

where:
F = Flux of impinging atoms
a = Substrate lattice constant
υ = Prefactor for diffusion
E_{Diff} = Activation free energy for diffusion
R = Gas constant
T = Temperature

From this formula it is clearly to see that the saturation density of nuclei increases with the vapor flux and the activation free energy of diffusion, whereas it decreases with increasing temperature and diffusion prefactor.

Heterogeneous nucleation is nucleation on a non-perfect surface. Surfaces can have many different kinds of defects. There are intrinsic defects like steps, kinks and terraces and extrinsic defects like adatoms, clusters and vacancies. Every real surface has some defects, so that perfect homogeneous nucleation is only hypothetical. Surface defects often serve as a nucleation center, since diffusing adatoms have a longer residence time

at the defects. Therefore nucleation is much more probably at defects. If the density of defects on a surface is high enough, the density of nuclei N is equal to the density of defects. In this case the saturation density of nuclei depends on no other parameter.

Even if it was possible to apply some thermodynamical considerations to thin film growth, it still is a non-equilibrium process which is governed by kinetics. One important kinetic factor for nucleation and growth on a heterogeneous surface or beyond the first layer is the Ehrlich-Schwoebel or step-edge-barrier. It was first observed in 1966 by Ehrlich [21] and theoretically explained by Schwoebel three years later [22]. It is both an energetic and physical obstruction for diffusion near step-edges. As it is shown in Fig. 3.3, an atom diffusing on an upper layer might be reflected from a descending step edge, since it can not overcome the Ehrlich-Schwoebel barrier. There is also a distinctive energetic feature at ascending step edges. An effective trap-site at ascending step-edges has important physical consequences, like step-flow growth in molecular-beam epitaxy.

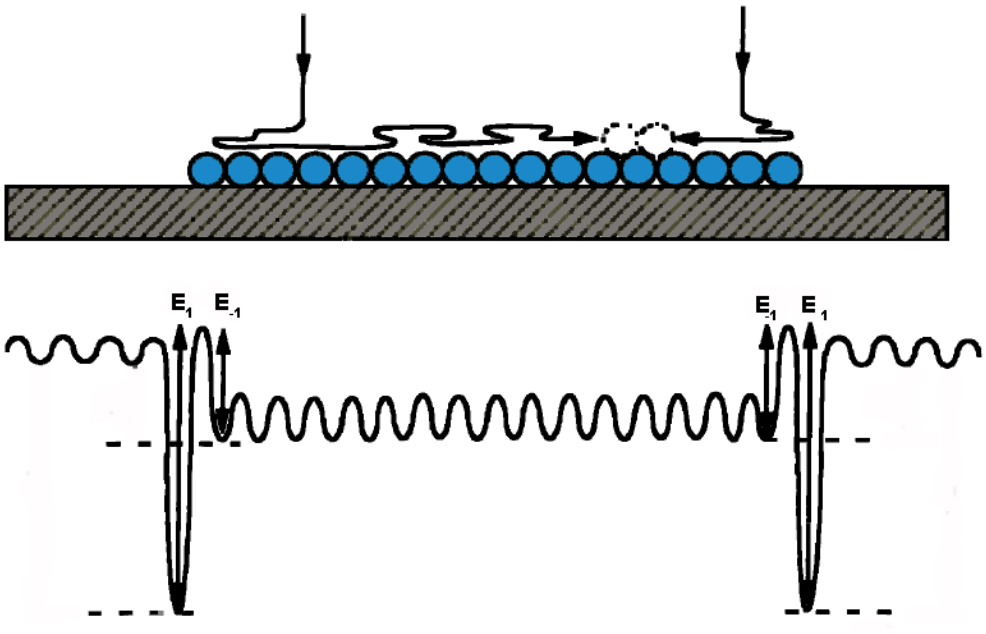

Figure 3.3: Ehrlich-Schwoebel barrier for adatoms on a substrate layer [23]. The barrier for downstepping is E_{-1}, the trap-site for upstepping it is E_1

Summarized, nucleation and growth are two phenomena that lead to thin film growth. Diffusing adatoms build nuclei on a surface. They become stable if a critical cluster size is reached. The number of stable nuclei on the surface increases until a saturation density of nuclei N is reached. By attaching more and more adatoms the stable nuclei become bigger and a thin film of adatoms grows on the surface. Three different fundamental growth modes are distinguished, whereas the real growth modes may be all kind of mixtures of the three fundamental modes.

Chapter 4

Adsorbate induced faceting

Faceting is the process when an initially planar surface converts into a "hill and valley" crystal surface. Adsorbate induced faceting is a form of self-assembly on adsorbate-covered single crystal surfaces, which is thermodynamically driven as it involves the mass transport of a large number of atoms. It is limited to a nanometer scale because of limitations in mass transport.

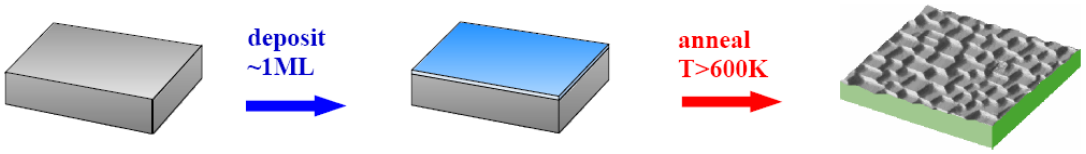

Figure 4.1: The schematic of adsorbate-induced faceting.

Faceting is usually discussed in the context of thermodynamically equilibrium. In this equilibrium, a crystal will seek the "Equilibrium Crystal Shape" (ECS) , which is determined by the minimization of the integral $\oint \gamma(\vec{n})da$, whereby γ is the surface free energy per area and da is an infinitesimal small part of the surface area. The driving force for surface faceting is the anisotropy of the surface free energy, which is defined as $\frac{\Delta\gamma}{\gamma}$. When a planar surface forms facets the total energy of the faceted surface must be smaller than that of the original surface, so that a faceted surface is energetically more favorable. For clean metal surfaces, the anisotropy of the surface free energy is generally too small to cause faceting. Even atomically rough surfaces, which in principle have a higher surface free energy than close-packed surfaces, still remain in their original

orientation after annealing. However, it is well known that the anisotropy of surface free energy can be enhanced by covering the surface with an adsorbate. As a result, a clean surface that is originally planar, when annealed, might undergo faceting to reduce the total surface free energy. This process is called adsorbate-induced faceting (Figure: 4.1).

Oxygen induced faceting of Re ($12\bar{3}1$)

Within this thesis a rhenium crystal with the orientation ($12\bar{3}1$) is used as a substrate. The orientation ($12\bar{3}1$) is an especially interesting surface on which to study adsorbate induced faceting for two reasons. First, Re ($12\bar{3}1$) is an atomically rough surface with six layers of atoms exposed (Figure: 4.2), so it has a high surface free energy relative to more close-packed Re surfaces. Therefore there is a high probability that faceting may be induced on this surface. Second, as shown in the stereographic projection (Figure: 4.2), the ($12\bar{3}1$) surface is near to several more closed packed surfaces. For these generally more stable surfaces, such as ($11\bar{2}0$), ($01\bar{1}0$), ($01\bar{1}1$) and ($11\bar{2}2$), it is very like to appear as facets on the Re ($12\bar{3}1$) surface .

The morphological evolution in oxygen induced faceting of Re ($12\bar{3}1$) was studied extensively by Hao Wang et al.[24]. Indeed it was found that Re ($12\bar{3}1$) shows a broad variety of different facets. There is a quite complicated morphological evolution of facets on Re ($12\bar{3}1$) ranging from long sawtooth ridges to complex structures exposing four different facets, depending on the oxygen coverage of the surface (Figure: 4.3). Faceting only occurs when the oxygen coverage (θ) exceeds 0.5 monolayer (ML) and the surface is annealed above 700 K. At low oxygen coverage (0.5 ML $< \theta <$ 0.7 ML) a partially faceted surface is observed upon annealing. Further increasing of the oxygen coverage (0.7 ML $< \theta <$ 0.9 ML) produces a completely faceted surface with long sawtooth ridges along the [$\bar{2}113$] direction. The typical dimensions of these ridges are $\sim$ 8 nm in width and $>$ 50 nm in length upon annealing to 1000 K, whereby the size of the ridges grows

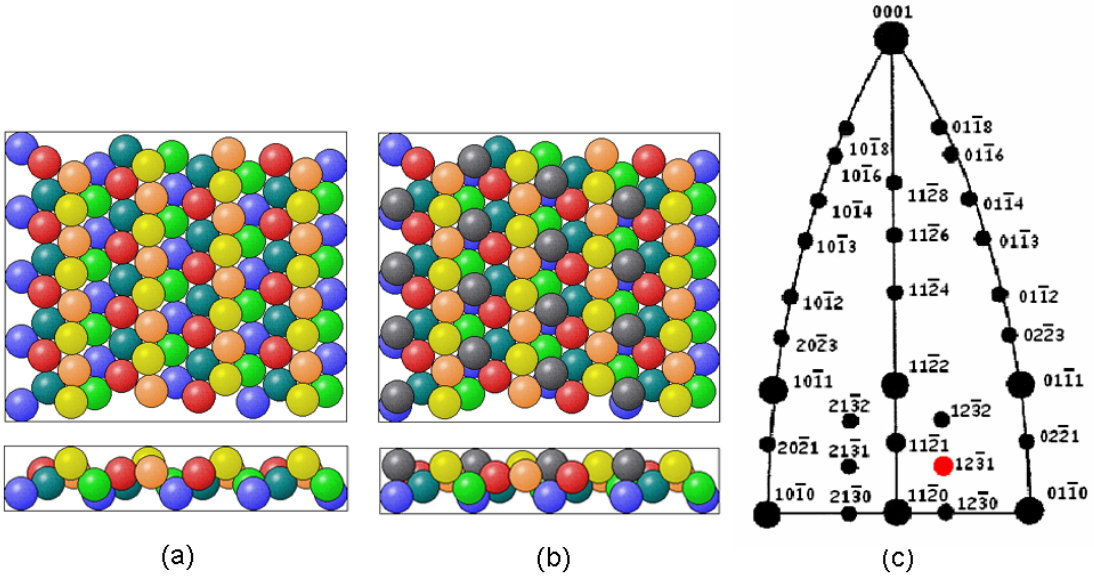

Figure 4.2: (a) A hard-sphere model of the Re (12$\bar{3}$1) surface. (b) The other stacking sequence of the Re (12$\bar{3}$1) surface with one more layer of atoms added on top of the surface in (a). (c) The stereographic projection of the hcp lattice on the plane (11$\bar{2}$0). The (12$\bar{3}$1) surface is labeled by a red dot.

with the annealing time and temperature. The two sides of the ridges were determined as (01$\bar{1}$0) and (11$\bar{2}$1) orientations. At an oxygen coverage between 0.9 ML and 1.0 ML a third set of facets occurs with (10$\bar{1}$0) orientation. These facets truncate the original ridges and therefore decrease the average ridges length in the [$\bar{2}$113] direction. With the surface fully covered (θ = 1.0 ML) a fourth facet, (01$\bar{1}$1), appears upon annealing, forming a quite complex surface structure. The whole morphological evolution is accompanied by a reduction of the average length along the [$\bar{2}$113] direction. This indicates that the (11$\bar{2}$1) facet is metastable.

Oxygen-Coverage (ML)	**Facets**
$\theta < 0.5$	planar
$0.5 < \theta < 0.7$	partially faceted
$0.7 < \theta < 0.9$	(01$\bar{1}$0), (11$\bar{2}$1)
$0.9 < \theta < 1.0$	(01$\bar{1}$0), (11$\bar{2}$1), (10$\bar{1}$0)
$\theta = 1.0$	(01$\bar{1}$0), (11$\bar{2}$1), (10$\bar{1}$0), (01$\bar{1}$1)

Table 4.1: Facet formation, depending on the oxygen coverage

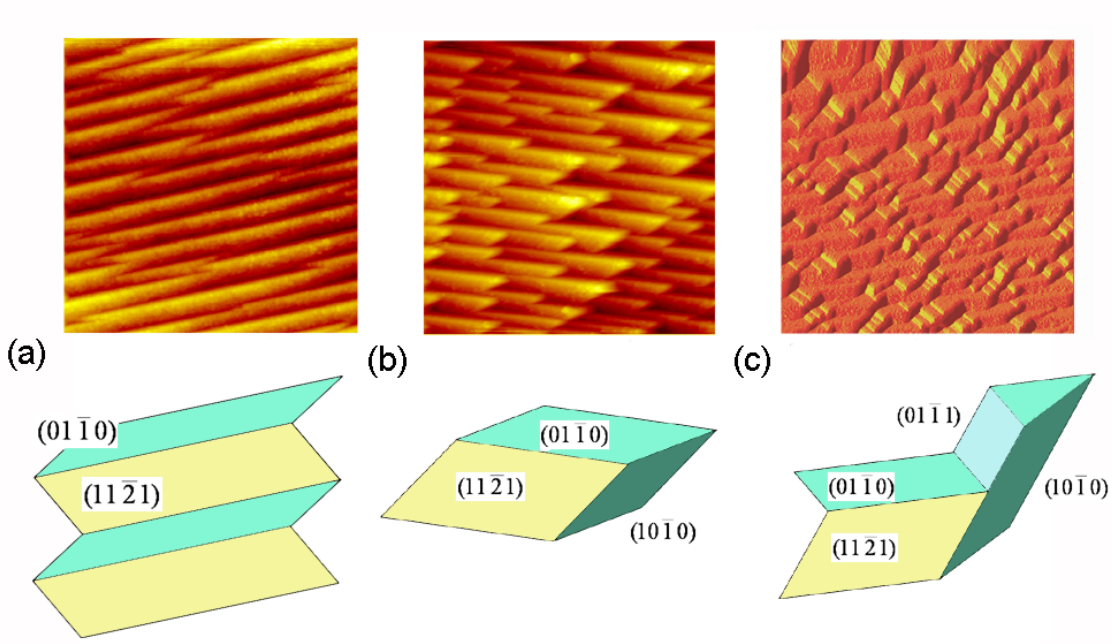

Figure 4.3: STM-Images and graphics of the morphological evolution of faceting on the Re (12$\bar{3}$1) surface [29]. All images are 100 nm × 100 nm, annealing temperature is 1000 K. (a): $\theta = 0.7$ ML ; (b): $\theta = 0.9$ ML ; (c): $\theta = 1.0$ ML ; x-slope image

All surface structures mentioned in Hao Wang's article [24] were obtained by the same experimental routine. Oxygen was dosed on the rhenium surface at room temperature by backfilling the chamber. Afterwards the sample was annealed to the to the required temperature.

For this work the focus is on the two sided ridges that were observed for an oxygen coverage between 0.7 monolayer and 0.9 monolayer (Figure: 4.3 a). To obtain the best results within this work it is desirable to have the size of the ridges as big as possible. Coincidently it was found that flashing the rhenium sample in oxygen atmosphere and allowing the sample to cool down in it creates bigger two sided ridges than the method mentioned above. This is why the routine used to create the two sided ridges within this thesis is a little bit different from the one described in Ref. [24]. More details about the structure of the two sided ridges and the experimental routine used to create them are given in the experimental chapter (Section: 6.1.1).

Chapter 5

Experimental techniques

All experiments described in this thesis were performed inside the same stainless steel ultra high vacuum (UHV) system. It consists of four separate chambers (main chamber, preparation chamber, STM chamber, introduction chamber) which are connected with each other. It is possible to isolate the preparation chamber from the other chambers with gate valves. So it is possible to prepare the sample inside the preparation chamber without contaminating the whole system. Also it is possible to introduce new samples through the introduction chamber without braking the vacuum inside the other chambers. This is very timesaving, as it takes around 60 hours to pump the whole system to UHV conditions (Section: 5.1). For sample transportation between the individual chambers, three different manipulators/translators are utilized. One large translator allows the transport between the preparation chamber and the main chamber. A manipulator and an additional wobble stick are used for the sample transport inside and between STM chamber and main chamber. Another translator is applied between preparation chamber and introduction chamber.

In the preparation chamber an argon source, an oxygen source and an ion-gun are located. There is also a facility for heating the sample via radiation and electron bombardment. In the main chamber low energy electron diffraction (LEED), Auger electron spectroscopy (AES) and a gold source are situated. An Omicron scanning tunneling microscope (STM) is located in the STM chamber. A schematical drawing of the whole UHV-system is shown in Fig. 5.1.

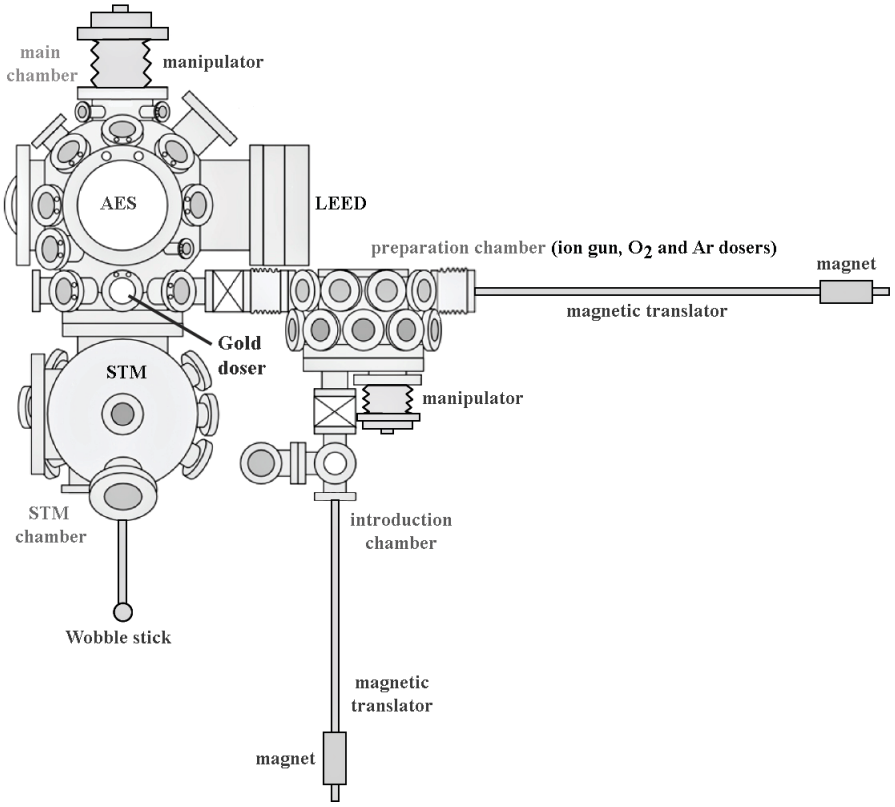

Figure 5.1: Schematical drawing of the UHV-system used for this studies [25]

5.1 Ultra high vacuum (UHV)

All experiments described in this thesis require ultra high vacuum conditions. Ultra high vacuum is the vacuum regime with pressures below 1.0×10^{-8} Torr[1]. Under UHV-conditions, the number of particles is very low ($< 10^9$ molecules/cm^3). Therefore the mean free path for for particles is very long (> 1 km). The experimental techniques used within this thesis use charged particles (electrons) to obtain information about the surface. Since electrons interact strongly with gas molecules a long free mean path is mandatory, so that the electrons do not interact with residual gas molecules during the measurements. UHV conditions are also necessary to maintain the cleanliness of the

[1] 1 Torr = 133.322 Pascal

sample during the experiments. Small impurities on the surface can influence the experimental results strongly, as they can act as nucleation center for impinging adatoms, for example.

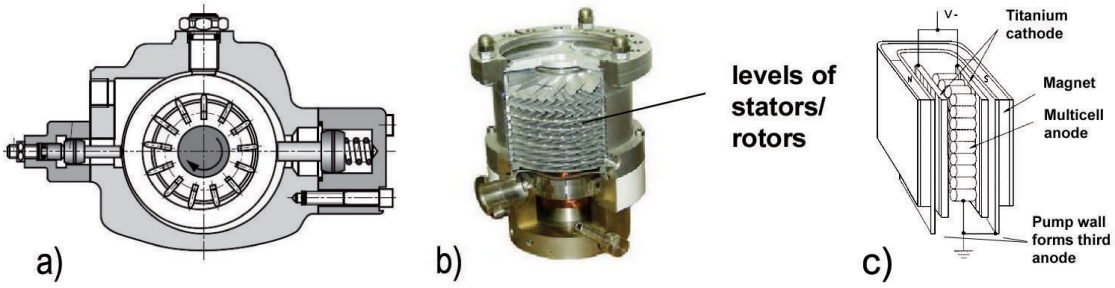

Figure 5.2: a) Schematics of a rotary pump ; b) cut trough a turbomolecular pump ; c) Schematics of an ion pump

The ultrahigh vacuum was obtained through a combination of different pumps. A mechanical rotary pump, a turbomolecular pump, an ion pump and a titanium sublimation pump were used to create the vacuum. First, a mechanical rotary pump was used to maintain a basic vacuum of about 1 mTorr. A rotary pump consists of a stator and an eccentric rotor which has two blades in a diametral slot. The whole stator-rotor assembly is submerged in a suitable oil. By drawing air from the vacuum chamber, compressing this air and evacuating it, the pump creates a low local pressure. (Figure: 5.2 a) The next step towards ultra high vacuum is a turbomolecular pump (Figure: 5.2 b). Turbomolecular pumps require a fore-vacuum to start pumping. Otherwise, they would overheat due to air friction. Modern turbomolecular pumps contain alternate axial stages of rotating and stationary discs and plates, which are cut with slots set at an angle so that gas molecules caught in the slots of the moving discs are projected preferentially in the direction of the slots in the stationary plates. The rotation speed of a modern turbomolecular pump is around 1500 Hz. Therefore the rotors velocity is in the same range as the mean thermal velocity of the gas molecules, so that they can transfer a maximum

momentum to the molecules and accelerate them into the direction of the next stationary plate. By running both a mechanical rotary pump and a turbomolecular pump for around 12 hours a pressure around 5.0×10^{-7} Torr is achieved. At this pressure the ion pump can be started. Ion pumps consist of two parallel, titanium covered stainless steel walls which act as a cathode. Between these two walls there are several stainless steal cylinders acting as anodes (Figure: 5.2 c). A potential difference of about 6000 V is maintained between the electrodes and causes electrical discharge. Electrons are emitted from the walls and guided in flat helical paths by a magnetic field ($\approx$ 0.15 T) normal to the cathode walls. If the ejected electrons hit gas molecules they ionize them. Due to the electric field this ions are accelerated towards the titanium walls, where they are caught by chemisorption. The impact of the ions on the wall causes emission of titanium atoms from the wall. These titanium atoms also chemisorb gas molecules and therefore increase the pumping speed [26]. After running the rotary pump, turbomolecular pump and ion pump for around 24 hours a pressure below 1.0×10^{-8} Torr is reached.

In order to further reduce the pressure it is necessary to remove the water vapor inside the chamber. This is achieved by "baking" the UHV-system. Baking means heating the chamber to temperatures between 150° C and 250° C for 24 to 36 hours in order to desorb molecules from the walls of the chamber. At the end of the baking procedure it is necessary to degas all filaments inside the vacuum chamber. Since the walls of the chamber are still hot the released contaminations do not stick on the walls but can be removed by the pumps. Now the titanium sublimation pump (TSP) is used to reduce the hydrogen level inside the chamber. Thereby titanium atoms are evaporated by passing a high current ($\approx$ 50 A) through a titanium rod. The released titanium atoms are very reactive and "pump" the chamber by chemisorption of gas molecules. After the UHV-system has cooled down completely, the pressure of the system should be around 2.0×10^{-10} Torr. This is the base pressure that was used to perform the experiments.

5.2 Low energy electron diffraction (LEED)

Low energy electron diffraction (LEED) is a technique which is used in surface science for the determination of surface structures, whereby a well defined low energy electron beam is shot onto well ordered crystal surface. The elastically backscattered electrons are now collected by a fluorescent phosphor screen, which is placed behind the electron gun (Figure: 5.3). Due to constructive interference of electron-waves a pattern of interference maxima develops on the screen. As it is shown below, this pattern also matches the crystal reciprocal lattice. Therefore it is possible to get information about the crystal surface structure by analyzing the LEED pattern.

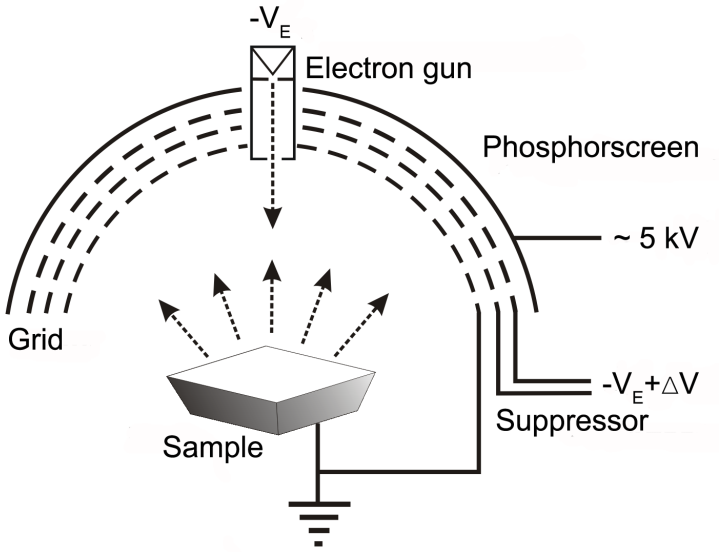

Figure 5.3: Schematics of a LEED experiment. The different grids are used to suppress the non-elastic scattered electrons, so that only elastic scattered electrons reach the phosphor screen.

The fundamental idea behind LEED is the wave-particle dualism of quantum mechanics, which says that electrons have both particle and wavelike nature. If you consider the wavelike nature of electrons you can think about electron diffraction. The electrons

wavelength is given by the de Broglie relation (5.1) [27]:

$$\lambda = \frac{h}{p} \tag{5.1}$$

where λ = wavelength , h = Planck constant , p = momentum.

With $p = \sqrt{2 \cdot m \cdot E_k}$ we finally get:

$$\lambda = \frac{h}{\sqrt{2 \cdot m \cdot E_k}} \tag{5.2}$$

where m = electron mass , E_k = electron energy.

From formula (5.2) you can see that the electron wavelength decreases with increasing electron energy. For electron diffraction you need an electron wavelength in the range of atomic spacing. This is achieved by using electron energies between approximately 20 eV - 300 eV for LEED experiments, which leads to electron wavelengths between 2.7 Å - 0.9 Å.

Elastic scattering of electrons is highly surface sensitive. Electrons are charged particles and therefore interact strongly with other particles. Their mean free path inside a solid is only a few Angstrom. The major interaction mechanism between electrons and the solid is the excitation of plasmon waves. Since plasmons appear in all kind of metals, the dependency of the mean free path from the electron energy is similar for many metals. This "universal" dependency is shown in Fig. 5.4. There you can also see that the minimum of the mean free path matches the electron energies used for LEED measurements; another reason for the surface sensitivity of LEED.

The short mean free path in solids allows us to treat the electron diffraction as a 2D problem. Considering the electron incidence from the normal direction, which is the case in LEED-experiments, the electrons scatter from the surface with an angle γ with respect to the surface normal. The condition for constructive interference between

different electron waves, which is also known as Bragg condition, is :

$$a_i \cdot sin(\gamma) = l \cdot \lambda \tag{5.3}$$

where a_i is the lattice constant of the crystal, l is an integer number and λ is the electron's wavelength (Figure: 5.5).

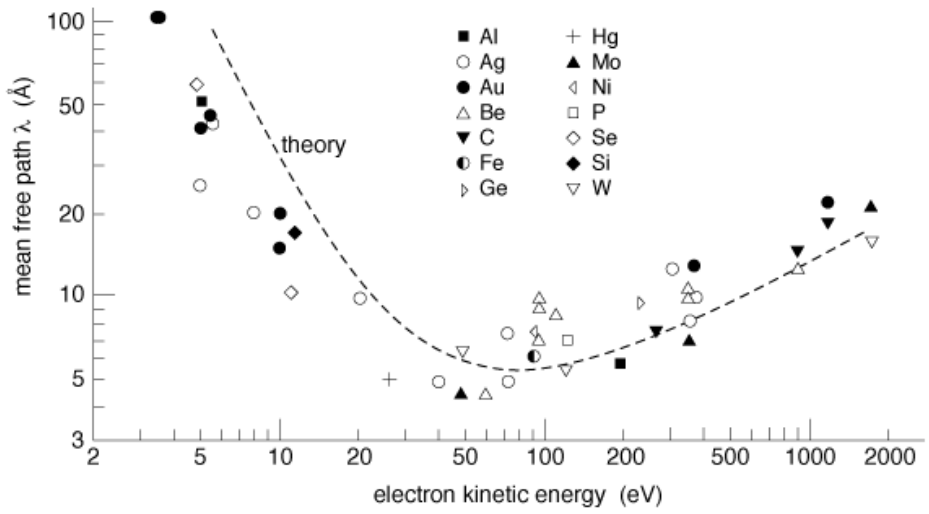

Figure 5.4: Mean free path of electrons in different metals versus electron energy. The dots are measurements, the dashed curve is a calculation. [18]

Using the relation $\lambda = \frac{2\pi}{K}$, the conditions for interference maxima in 2D are:

$$\vec{a_1} \cdot (\vec{K_{out}} - \vec{K_{in}}) = 2\pi \cdot n \tag{5.4}$$

$$\vec{a_2} \cdot (\vec{K_{out}} - \vec{K_{in}}) = 2\pi \cdot m \tag{5.5}$$

where $\vec{a_i}$ are the real space lattice vectors of the crystal, $\vec{K_{in}}$ and $\vec{K_{out}}$ the incoming and outgoing wave vectors of the electrons and n and m are integer numbers.
If one now remembers the defining relationship for the reciprocal space, $\vec{a_i} \cdot \vec{b_j} = 2\pi \cdot \delta_{ij}$, where $\vec{a_i}$ is a real space vector and $\vec{b_j}$ is a vector in reciprocal space, it is obvious that the equations (5.4) and (5.5) are satisfied if:

$$\Delta\vec{K} = (\vec{K_{out}} - \vec{K_{in}}) = n \cdot \vec{b_1} + m \cdot \vec{b_2} \tag{5.6}$$

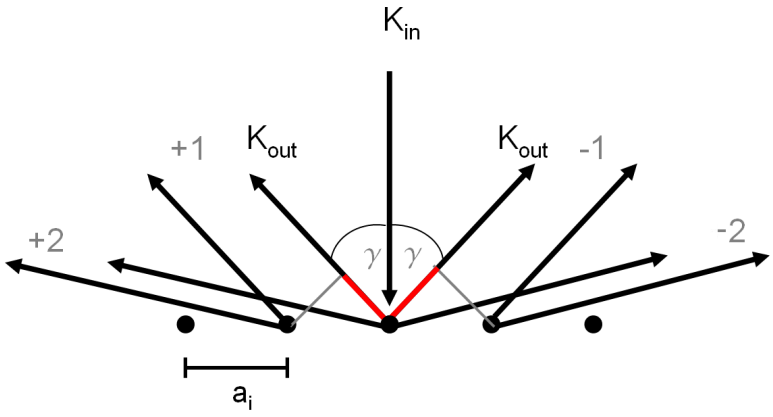

Figure 5.5: The incident wave vector K_{in} (perpendicular incident on the sample) and the outgoing wave vectors K_{out} for the first and second order interference maxima.

Since $\vec{b_i}$ are vectors of the reciprocal space, $\Delta\vec{K}$ is also a 2D reciprocal lattice vector. Therefore the LEED-pattern, which corresponds to the interference maxima, is an image of the crystal reciprocal lattice. Knowing this, LEED offers a huge variety of different applications to understand the surface structure of a crystal, like determining facets-orientations or detecting reconstructions on the surface [28].

LEED is also very convenient just to quickly check if a surface is faceted or not. If we combine the formulas (5.2) and (5.3) we get:

$$sin(\gamma) = \frac{h \cdot l}{\sqrt{2 \cdot m \cdot E_k} \cdot a_i} \tag{5.7}$$

From formula (5.7) you can see that all LEED spots on a planar surface will move towards normal direction with increasing electron energy (this is also the position of the specular beam for a planar surface). For a faceted surface the situation is different. The spots of the LEED pattern will not longer move towards normal direction, but they still move towards the specular beam direction, as shown in Fig. 5.6. The specular beam obeys the laws of linear optics (angle of incidence = angle of reflection). Therefore there is one specular beam and one set of LEED spots for every surface facet. Thus it is very easy to judge if a surface is faceted. If all LEED spots on the screen move towards the center position, the surface is still planar. If there are spots on the screen that do

not move towards the center, these spots correspond to surface facets. An analysis of the motion of these spots can also gives a rough idea about the arrangement of the facets. Since the spots will move to the facet's specular beam it is possible to find out the position of the specular beam. As the specular beam obeys optical laws, it provides information about the facet orientation.

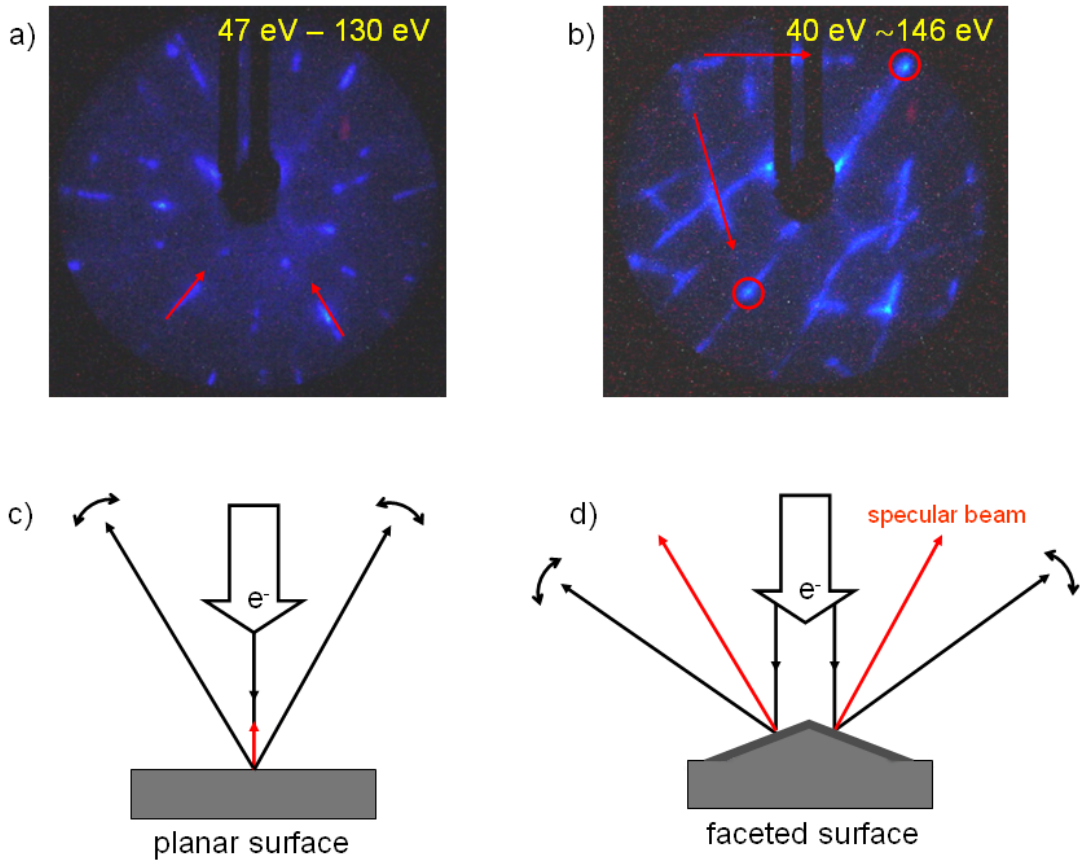

Figure 5.6: Identification of surface structures by LEED. [29]
a) LEED pattern of a planar surface structure. Electron energy: 47 eV - 130 eV.
b) LEED pattern of a surface structure consisting of two sided ridges. The specular beam spots are marked by red circles. Electron energy: 40 eV - 146 eV.
c) Schematics of the motion of LEED spots on a planar surface.
d) Schematics of the motion of LEED spots on a faceted surface structure.

5.3 Auger electron spectroscopy (AES)

Auger electron spectroscopy (AES) is a very commonly used surface science technique for determining the chemical composition on the surface of a sample. It is based on the Auger-process (Figure: 5.7), which was discovered independently by Lise Meitner and Pierre Auger in the 1920's .

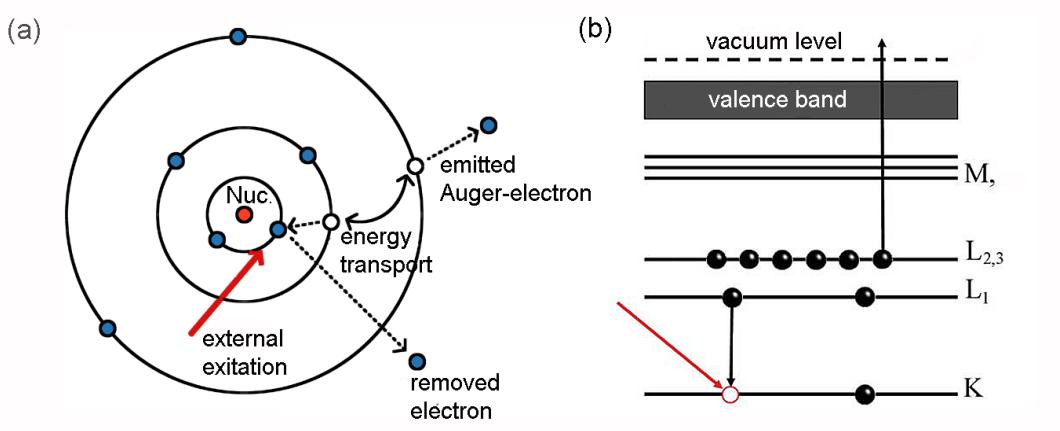

Figure 5.7: (a): Schematics of the Auger process in an orbital model. (b): Schematics of the Auger Process in an energetic model (KL_1L_{23} – transition). [30]

When an atom is ionized by the production of a core hole, whether by an incident photon or, as in AES, by an incident energetic electron beam, there are in general two possible physical processes for the atom to relax. One is by filling the core hole with an electron from a higher shell and the simultaneous release of a X-ray photon. However, this photon emission process is of little interest in surface science since the emerging photons have a long mean free path in solids and therefore the process is not very surface sensitive. The second process is the so called Auger process. Again, the core hole is filled by an electron from a higher shell. But now, in difference to the photon emission, the liberated energy is transfered to another electron in a higher shell. This so called Auger-electron also gets ejected from the atom due to the energy transfer (Figure: 5.7).

By ignoring relaxation of the atomic energy levels, the kinetic energy (KE) of the Auger-electron is [31]:

$$KE = E_A - E_B + E_C \tag{5.8}$$

where E_A is the binding energy of the core level electron (> 0), E_B is the binding energy of the electron that fills the core hole (> 0) and E_C is the ionization energy of the Auger electron (< 0). The kinetic energy of Auger-electrons is relatively low ($\sim$ 50 eV - 1000 eV) and they have a very short mean free path. So only Auger-electrons close to the surface can emerge from the solid. Consequently all information obtained by Auger electron spectroscopy comes from the surface, which makes AES is a very surface sensitive technique.

In AES-experiments, an electron beam in the range of $\sim$ 1.5 keV - 5 keV is directed onto a surface, causing the initial core hole of the Auger process. Since the energy-splitting of the atom orbitals is different for every element, the spectrum of emitted Auger-electrons is unique for every single element and therefore can be used as a fingerprint of the chemical composition of a surface. These spectrum usually comes on top of a large, linearly increasing electron background, which is caused by inelastic scattered electrons. Because of that it is common not to take the raw spectrum, which is the Auger-electron distribution N as a function of electron kinetic energy E, but the derivative of the spectrum, $\frac{dN}{dE}$, as the Auger spectrum. Tabulated characteristic Auger spectra of the different elements are available [32]. By comparing these tabulated spectra with the spectra obtained by Auger measurements of a sample it is possible to identify the chemical elements on the sample (Figure: 5.8). It is worth mentioning that the two lightest elements, hydrogen and helium, cannot be detected by AES. The Auger process involves three electrons, a core vacancy and two outer electron. Both, hydrogen and helium, therefore have not enough electrons for the Auger process to take place.

It is also possible to obtain information about the growth mode (Chapter: 3) of deposited atoms on a crystalline surface by monitoring the peak to peak height of the

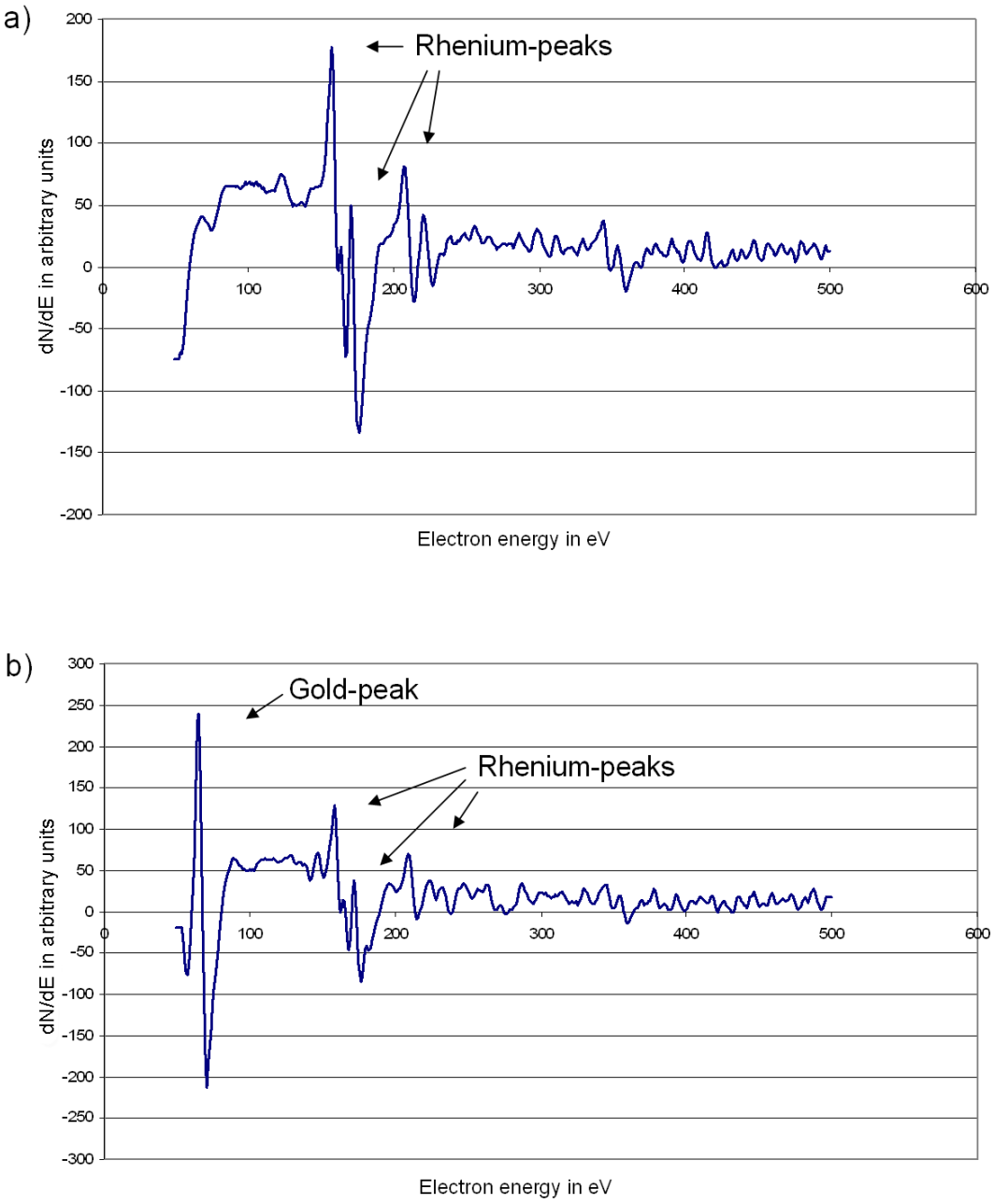

Figure 5.8: a) AES image of a clean Re $(12\bar{3}1)$ surface. The characteristic rhenium peaks are indicated with arrows.
b) AES image of a gold covered Re$(12\bar{3}1)$ surface. The gold coverage is about 1.4 ML. The characteristic peaks for rhenium and gold are indicated with arrows.

Auger signal from the overlayer as a function of coverage. The evolution of this quantity with overlayer thickness can be used to distinguish the different growth modes. Generally the deposit signal increases with the coverage until a saturation is reached. Saturation is reached when no more Auger-electrons from the substrate can penetrate the overlayer film and contribute to the Auger signal.

For Frank-van der Merwe growth, a linear increase in the overlayer Auger signal is expected until the first layer is completed. After this a new layer starts forming and another linear slope is expected; but due to attenuation by the first layer, the slope for the second layer will be lower. Consequently the trend of the peak to peak Auger intensity for Frank-van der Merwe growth shows linear sections, whereas the slope decreases after a new layer is completed (Figure: 5.9 a). For Volmer-Weber growth, a linear increase

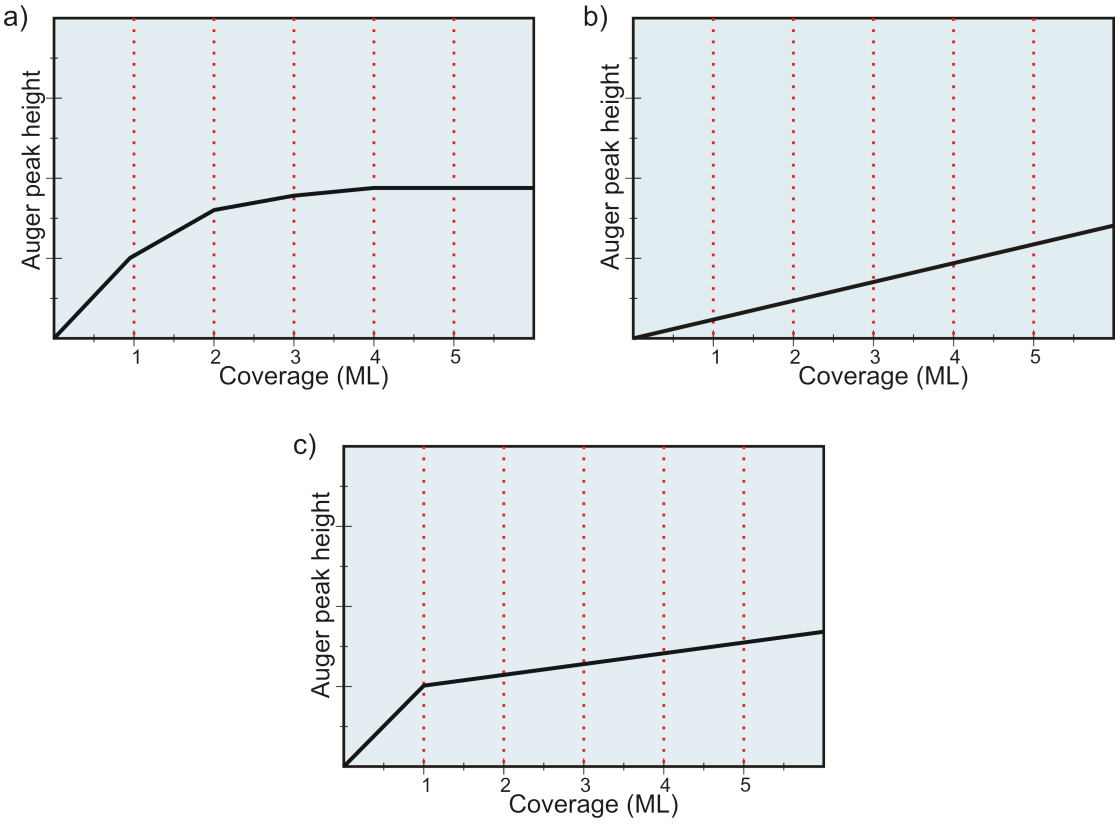

Figure 5.9: Evolution of Auger peak height as function of surface coverage for the three general growth modes.
a) Layer by layer growth ; b) Island growth ; c) Layer plus island growth

with low slope is expected until a saturation is reached. Since the adatoms do not wet the surface completely a monolayer is only a "hypothetical" coverage. Therefore no change in the slope is expected after the dose of one monolayer (Figure: 5.9 b). Stranski-Krastanov growth is a combination of both of the other growth modes. Therefore a combination of the both characteristics is expected. As long as the atoms grow in Frank-van der Merwe fashion the slope changes after a new layer is completed. When the growth mode switches to Volmer-Weber growth mode, the slope becomes very low and constant (Figure: 5.9 c).

5.4 Scanning tunneling microscopy (STM)

Scanning tunneling microscopy is an experimental technique used to image surface structures. Invented in 1981 by Gerd Binnig and Heinrich Rohrer it soon became one of the major techniques in surface science, winning its inventors the 1986 Nobel Price in Physics [33].

By scanning a conducting surface with an atomically sharp metal tip it is possible to relate the tunneling current between the surface and the tip to the geometric and electronic structures of the surface. Thereby it is possible to obtain images of the surface's real space structure. So it is possible to display non-periodic surface features like defects and impurities [34]. This is the big advantage of STM over scattering techniques like LEED; these techniques only provide information about the sample's reciprocal space structure. Therefore they are only capable of providing information about periodic structures.

The basic principle of scanning tunneling microscopy is the quantum mechanical concept of electron tunneling. When an atomically sharp metal tip approaches a conducting surface to distances of a few Angström and a small bias is applied between tip and surface a small current flows even if there is no physical contact between them (Figure: 5.10).

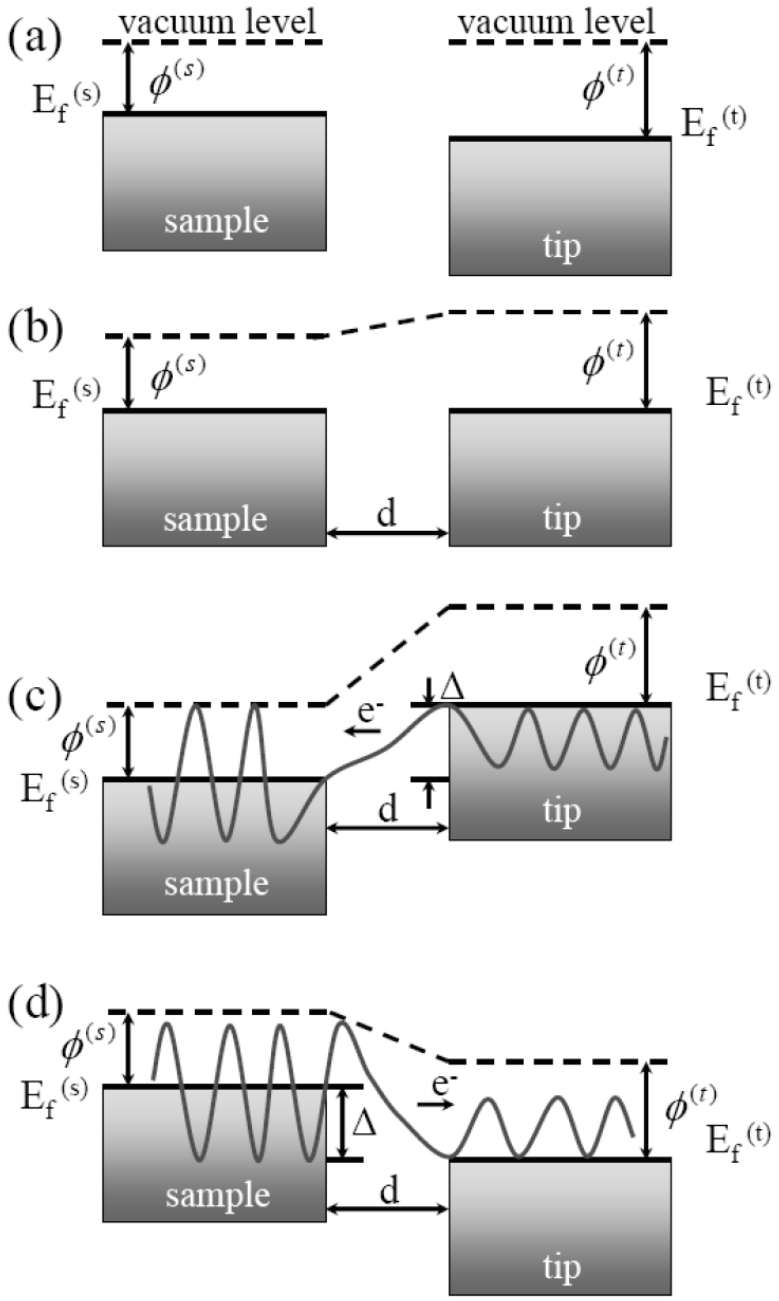

Figure 5.10: Concept of electron tunneling ($\phi^{(i)}$ are the workfunctions of surface and tip) [35]. (a): Tip and sample far apart, no interaction between them. (b): Tip and sample are brought close together. But there is now current flow, since there Fermi levels E_f^i are well aligned. (c) Now a bias is applied between tip (-) and sample(+). This bias (Δ) shifts the Fermi levels relatively to each other. Therefore, a current flow establishes. (d) The bias is inversed. Therefore the direction of the current flow changes.

In classical mechanics it is not possible for the electrons to overcome the vacuum-barrier between tip and surface. But in quantum mechanics there is a non-zero probability for the electron to tunnel through this barrier and establish a tunneling current. The full understanding of the theory of quantum tunneling applied on scanning tunneling microscopy is very hard; too many factors, like the shape of the tip or its electronic properties, influence the system and make it very challenging to develop a full theory. But even if you start with a simple one dimensional model with a potential barrier, that includes a small bias between sample and tip, it is possible to obtain a basic relationship for the tunneling current [36]:

$$I \propto V \cdot \rho_s(E_F) \cdot e^{-2 \cdot \kappa \cdot d} \tag{5.9}$$

where: V = Bias tip-sample ; ρ_s = surfaces local density of state at the Fermi level ; κ = decay constant ; d = distance tip-sample.

The important feature of (5.9) is the exponential relationship between the tunneling current I and the tip-sample distance d. This exponential distance-sensitivity of the tunneling current is used for scanning tunneling microscopy. You can also see from this formula that scanning tunneling microscopy does not really give a topographic image of the probed surface structure. Rather it gives an image of the surface density of state ρ_s. Therefore a careful interpretation of the STM data is necessary, since anomalies in the surface's electronic structure can influence the STM results significantly.

In a scanning tunneling microscope an atomically sharp metal tip (usually tungsten) is attached to a piezodrive, which consists of three mutually perpendicular piezoelectric transducers in x-,y- and z-direction. Upon applying a voltage the piezoelectric transducers expand or contracts, which allows to control the tip position very precisely. By using the z-piezo, the tip and the sample are brought within a few Angström of each other, so that a tunneling current is established. Now, by using the x- and y-piezos, the surface can be scanned (Figure: 5.11).

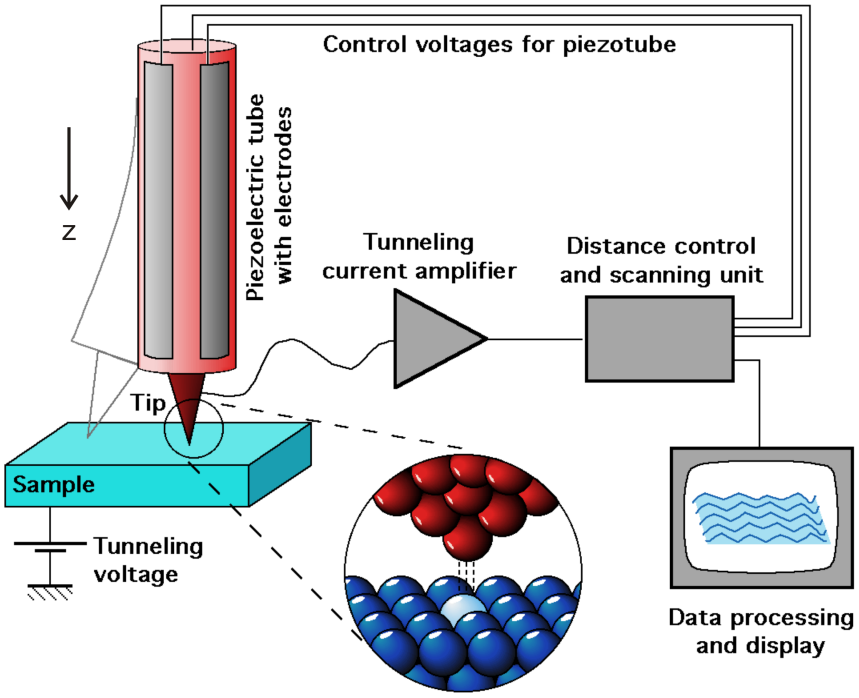

Figure 5.11: Schematic view of a STM setup

In general, there are two different modes of scanning a surface. In the "constant height" mode, the distance tip-sample is kept constant during scanning. By recording the modulation of the tunneling current as a function of the tip position it is possible to obtain information about the surface structure. This scanning mode allows to scan images very fast. But since the height is kept constant, only very smooth surface structures can be scanned. Otherwise, there is the danger of crashing the tip on some rough surface features (Figure: 5.12). The second scanning mode, which is used within this work, is the "constant current" mode. Here, the tunneling current is kept constant during the scanning of the surface. This is realized by a feedback loop that regulates the tip-sample distance. An analysis of the evolution of this distance during the scan finally provides an image of the surface structure.

The quality of STM-images depends on a variety of factors. On major factor are disturbances from the surrounding areas. To minimize this disturbances, the STM is

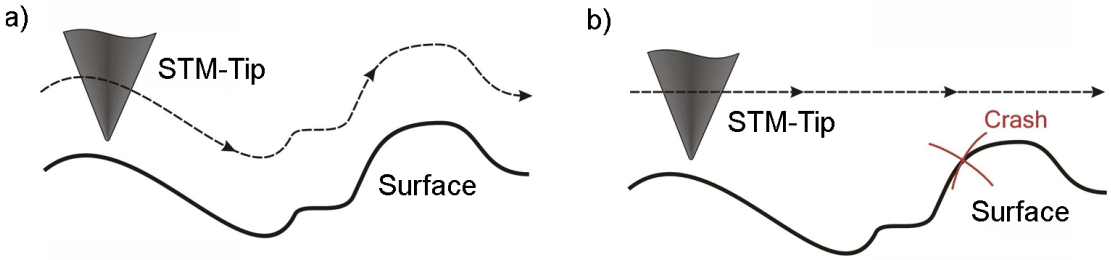

Figure 5.12: The different scanning modes of the STM.
a) Constant current mode ; b) Constant height mode

isolated from vibrations by a combination of springs and damping systems. Also the image quality is strongly affected by the quality of the used tips. In the ideal case the tip should only consist of a single atom. Even if this is not practical to achieve, the tip should be as sharp as possible. But still it is not necessary to purchase expansive STM tips. High quality tips can be produced without a huge effort by electrochemical etching. A method how to produce homemade STM tips by chemical etching is described in Appendix A.

Chapter 6

Experimental results

All experiments which are reported in this thesis were performed on the same rhenium single-crystal. The sample was $\sim$ 10 mm in diameter and $\sim$ 1.4 mm thick. Its purity was 99.95% and it was aligned within 0.5°of the $(12\bar{3}1)$ orientation.

All experiments were executed in the same manner. First, the rhenium sample was cleaned by annealing in the presences of oxygen and flash-heating in UHV. Flash-heating thereby means annealing of the sample to temperatures above 2000 K for 5 - 10 seconds and letting it cool down afterwards. The cleanliness of the sample was confirmed by Auger electron spectroscopy. If the experiment required an oxygen induced faceted surface, this facets now were created by flashing the sample whitin the chamber which was backfilled with oxygen. The development of the faceted surface was checked by LEED.

Following the preparation of the sample, the required amount of gold was dosed on the surface. The dose of gold was checked by AES again. STM images of the gold covered surface were taken, too. After this the sample was annealed to different temperatures and for different times by radiation heating. The change of the surface morphology due to annealing was monitored by low energy electron diffraction and especially scanning tunneling microscopy.

The results of this experiments are reported in this chapter. A detailed description of the single steps mentioned above is given below. Information about the oxygen induced faceting is given in the related segments. (Chapter: 4 ; Section: 6.1.1)

Sample cleaning

The cleanliness of the sample is very important for studies of the physical and electronic properties of a surface. Impurities of the sample can affect the experimental results strongly. They can influence nucleation as they might act as nucleation centers or they can change the experimental parameters. If carbon is left on the surface, for example, it can react with the oxygen dosed on the surface, thereby changing the concentration of oxygen on the surface.

The main impurities found during this experiments were carbon and nitrogen. To remove these impurities the sample was annealed in the presence of oxygen. To accomplish this the chamber was backfilled with oxygen to a pressure of 5.0×10^{-8} Torr, while the sample was annealed to a temperature around 1700 K for 3 minutes. Sample heating was achieved by electron beam heating. Here the sample was positioned over a tungsten filament. By applying a bias between this filament and the sample and using a current to anneal the filament, electrons were ejected by the filament and accelerated towards the sample[1]. After this oxygen treatment the sample was flashed several times in UHV to temperatures around 2100 K for 10 seconds[2].

Heating of the sample in UHV removes oxygen from the surface and also destroys all facets which have possibly built during the annealing in oxygen. Finally the cleanliness of the surface was confirmed by Auger electron spectroscopy.

Annealing the sample

In order to make a morphological change of the gold covered surface possible, annealing of the surface is necessary to provide enough energy to the atoms, so that they can overcome kinetic barriers and form new surface structures.

---

[1]Parameters: Bias (filament-sample): 1.25 kV ; Emission current (filament-sample): 50 mA

[2]Parameters: Bias (filament-sample): 1.25 kV ; Emission current (filament-sample): 90 mA

In these experiments, annealing of the sample was performed by radiation-heating. Therefore the same apparatus that is used for electron bombardment is also utilized here. The sample is fixed in a manipulator with a tungsten filament mounted below the sample. By passing a current trough the tungsten filament it is possible to anneal the sample. In contrast to the electron bombardment there is no bias applied between the sample and the filament. After a warm up time of around 10 minutes it is possible to reach sample temperatures up to 1000 K with this method. Here the current through the filament is up to 6 A. The sample temperature was monitored using an infrared pyrometer.

Depositing gold

The gold doser used during this experiments consists of a gold wire which is coiled around a tungsten filament. If a current flows trough this filament the wire gets hot. With the temperature of the wire its vapor pressure and therefore the number of ejected gold atoms increases. In order to get a reasonable dosing speed (1 monolayer/several minutes) a vapor pressure in the range of 10^{-6} Torr is required.

A particular problem of depositing gold is its low melting point of 1337 K. To reach the required vapor pressure temperatures around 1235 K are necessary for gold [37]. Hence the margin between the needed temperature and the melting temperature is very small. Thus it can happen that the wire changes its shape due to the high temperatures. So the doser which was used for this experiments changed its shape during the test run to a golden ball before it finally became stable.

In order to avoid changes of the doser shape and to assure a constant flux a precise adjustment of temperature and hence the current through the tungsten filament is very important. This was achieved by monitoring the current with a digital multimeter. The current which was used to anneal the gold was 2.35 A during all experiments.

Obtaining STM images

Most of the experimental results which are reported in this thesis were obtained by scanning tunneling microscopy. In order to get qualitatively good STM images it is necessary to find a combination of tunneling current and bias that fits with the used materials. For all STM images shown in this work the used tunneling current was between 0.8 nA and 1.6 nA and the bias was 1.0 V - 1.6 V.

A very important factor to get good images is the cleanliness of the STM tips. During the experiments it is possible that the tip picks up some contamination from the surface. This will influence the quality of the images strongly. One proper method to clean the tip is to "burn" it, which means keeping the tip fixed at one point and increasing the tunneling current and bias up to the maximum. Thus the tip will get hot and unwanted particles may desorbe from it. Another method of cleaning the tip is scanning a surface very quickly. So the tip may crash some surface area and thereby loose some atoms to become atomically sharp again.

Also it was found during the experiments that the best image quality was obtained during nighttime. This can be understand since at this time the general noise level from the surrounding area is lower. Therefore it is recommended to prepare the sample during daytime and scan the sample during nighttime.

6.1 Gold deposition on a faceted Re $(12\bar{3}1)$ surface

In the following sections a faceted rhenium sample is used as a template. The template's structure consists of two sided ridges, which are created by oxygen induced faceting. The fact that these ridges are relatively easy to create in a large scale on the Re $(12\bar{3}1)$ surface and their long term- and temperature-stability make this structure to a perfect template to study faceting phenomena on.

Within the following sections, the facets morphology is studied and the influence of gold deposition on top of it is reported.

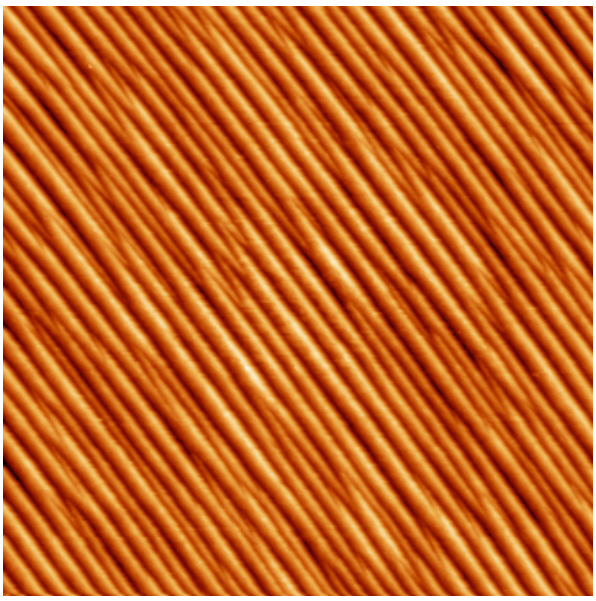

Figure 6.1: 500 nm × 500 nm STM image of the faceted Re $(12\bar{3}1)$ surface that is used as a template for the following experiments. The long range order of the structure is clearly visible.

6.1.1 Oxygen induced ridges on Re $(12\bar{3}1)$

The faceted surface that is used as a template is created by oxygen induced faceting. To induce the facets the sample was flashed in the presence of oxygen and allowed to cool down in this atmosphere afterwards. Here the preparation chamber of the system was

backfilled with oxygen to a pressure of 5.0×10^{-8} Torr and the sample was heated by electron bombardment to temperatures above 2000 K for around 10 seconds[3]. In this way two sided ridges were created on the surface.

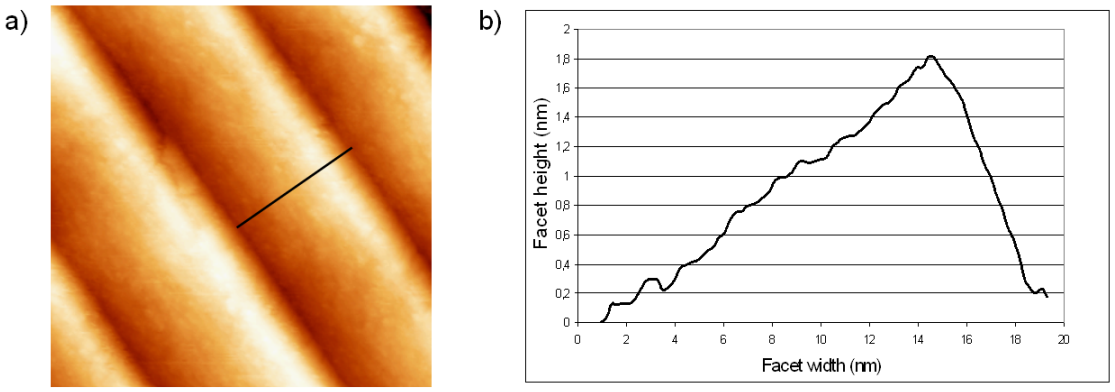

Figure 6.2: a) 50 nm × 50 nm STM image of the faceted Re surface ; the black line indicates the direction of the line profile in b) ;
b) Line profile of one facet in a)

The ridges, created in this manner, have an average width between 15 nm and 20 nm and an average height of 1.4 nm - 2.0 nm (Figure: 6.2). It is worth mentioning that the size of the ridges can be varied by changing the flashing temperature and time.

As reported in Ref. [24], the ridge's direction is $[\bar{2}113]$ and the orientations of the exposed facets are $(01\bar{1}0)$ and $(11\bar{2}1)$. $(01\bar{1}0)$ is a relatively stable surface with close-packed atomic rows. The distance between two neighboring atomic rows is d = 5.17 Å. $(11\bar{2}1)$ shows a quasihexagonal surface structure with lattice constants a = 5.24 Å and b = 5.17 Å and four atomic layers exposed (Figure: 6.3),this facet was found to be metastable. No reconstructions occur on either of the facets [24].

The tilt angle between the $(01\bar{1}0)$ facet and the $(12\bar{3}1)$ surface was calculated to be 22.6 °. The $(11\bar{2}1)$ facet has a tilt angle of 12.2 ° relative to the $(12\bar{3}1)$ substrate. Due to the faceting the surface area increases:

$$A_{faceted} = 1.04 \cdot A_{planar}$$

[3]Parameters: Bias (filament-sample): 1.25 kV ; Emission current (filament-sample): 80 mA - 90 mA

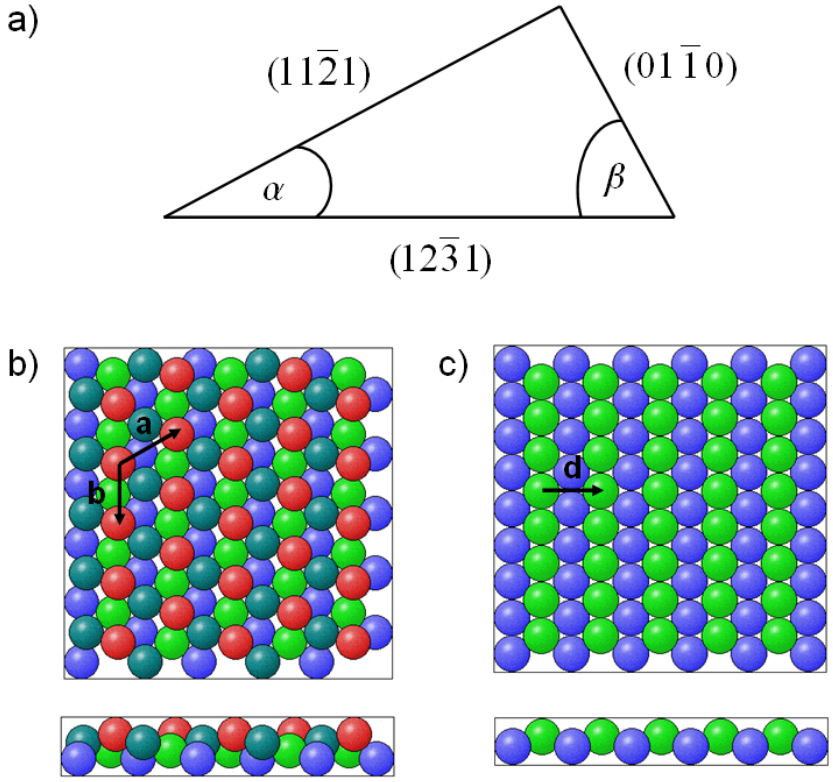

Figure 6.3: a) Schematics of the two sided ridges; $\alpha = 12.2°$, $\beta = 22.6°$
b) Hard-sphere model of the (11$\bar{2}$1) surface ; a = 5.24 Å , b = 5.17 Å
c) Hard-sphere model of the (01$\bar{1}$0) surface ; d = 5.17 Å

In order to confirm that the created facets really agree with the structure reported in Ref. [24], LEED measurements were performed. LEED clearly showed evidence for two sided ridges. Two sets of LEED-spots moving in different directions were found, corresponding to two different facets (Figure: 6.4 a). One specular beam spot was found on the screen. This spot was identified as the (11$\bar{2}$1) specular beam spot by analysis of its tilt angle and position on the LEED screen. The second specular beam spot was located outside the LEED screen. It was identified by analysis of the corresponding spots, which moved in the expected direction of the (01$\bar{1}$0) specular beam (according to Fig. 6.4 a). The position of this specular beam outside the screen is also plausible, since the tilt angle between (12$\bar{3}$1) and (01$\bar{1}$0) is much larger than that for (11$\bar{2}$1). Consequently the orientations of both the facets were confirmed as (01$\bar{1}$0) and (11$\bar{2}$1) by LEED.

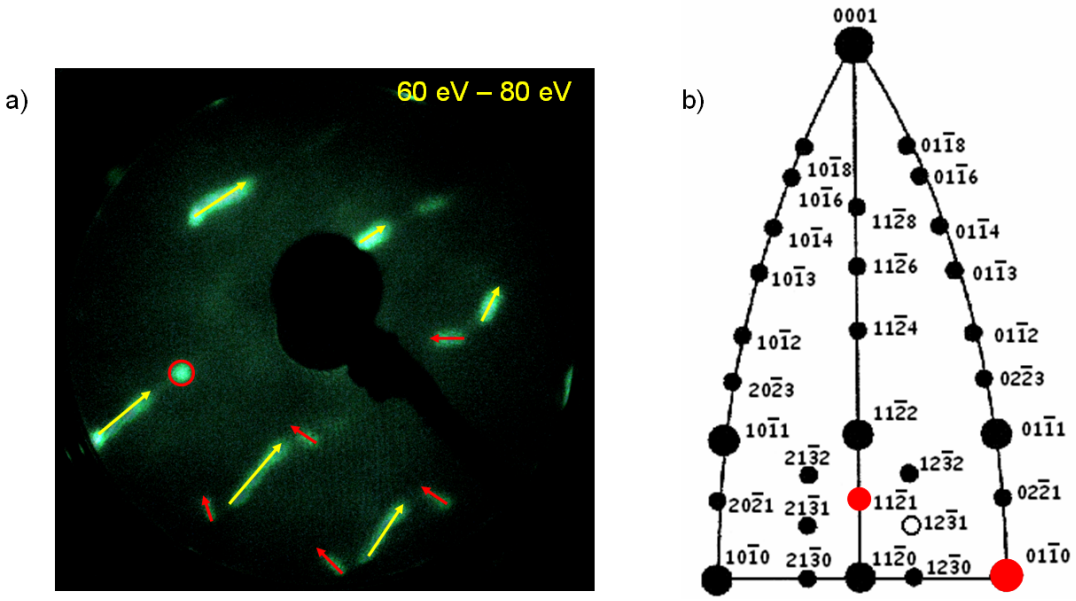

Figure 6.4: a) LEED image of the faceted surface. The motion of both sets of LEED-spots is marked with arrows. The (11$\bar{2}$1) spectral beam is marked by a red circle (Electron energy: 60 eV- 80 eV). b) Stereographic projection of the hpc lattice. The two facets in a) are marked by a red dot. The original (12$\bar{3}$1) substrate is marked by a black circle.

6.1.2 Gold nanoclusters on the faceted Re surface

After creating the oxygen induced ridges on the Re (12$\bar{3}$1) surface, gold was deposited on top of it. The question that occurs is in which way do the gold atoms grow on top of the faceted Re surface. To explore the growth mode, three different amounts of gold were deposited on the surface (1000 seconds dosing time ; 2000 seconds dosing time ; 3600 seconds dosing time). After the deposition, STM images of the gold covered surfaces were taken (Figure: 6.5).

From the STM images it is clear that the gold atoms grow in small clusters on top of the Re surface for all three gold coverages. It is also to see that the width of the gold clusters increases with the dosing time. The increase of the nanoclusters size with the coverage is reported many times for many different substrate/adatom systems [5]. Also this behavior can be understood easily, since there are more gold atoms available to build clusters with for higher coverage.

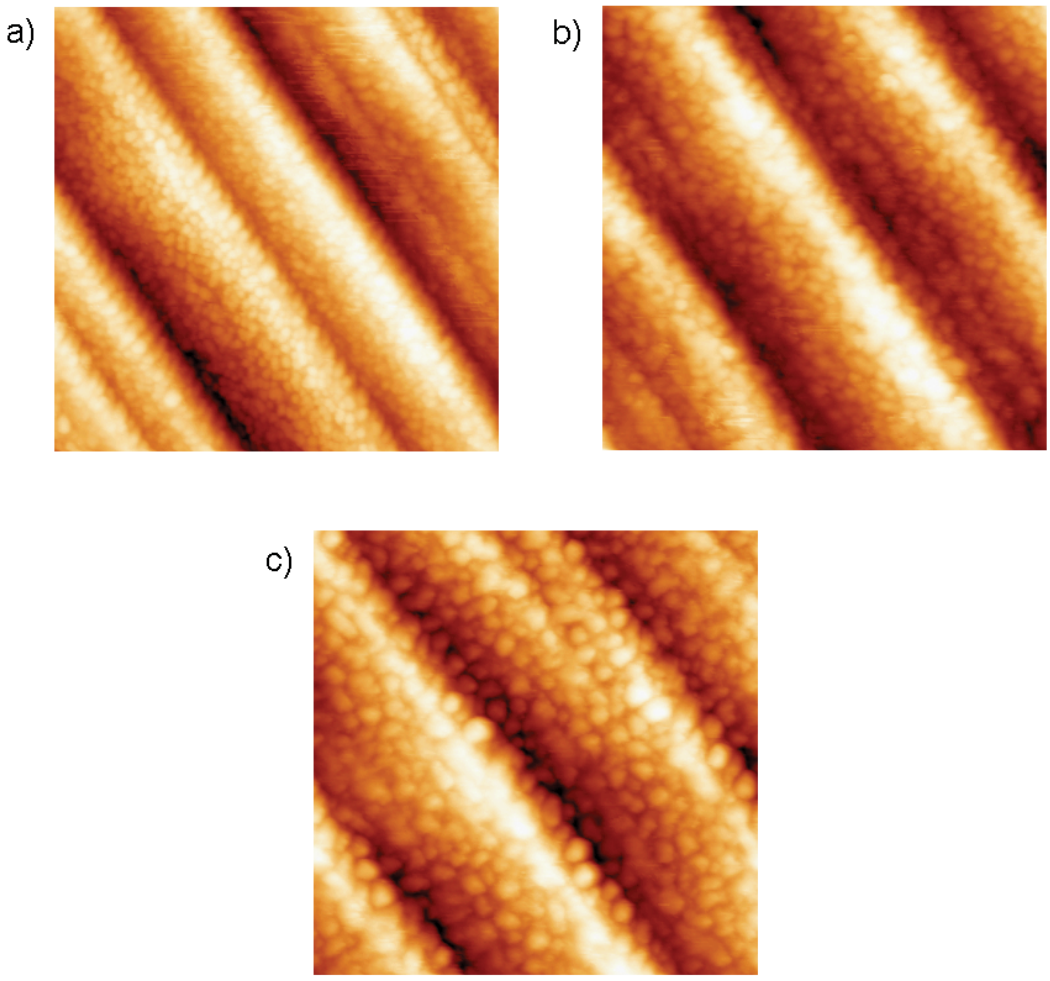

Figure 6.5: STM images of the gold covered Re surface (50 nm × 50 nm).
a) 1000 sec. dosing time ; b) 2000 sec. dosing time ; c) 3600 sec. dosing time

The average size of the gold clusters was obtained by using the line scan mode of the STM software. Many clusters were scanned for every coverage and the average was taken. The width of a cluster was defined as the length of the major axis of an elliptic cluster. (Table: 6.1)

One distinctive feature of the nanocluster's size is their height. For 1000 seconds and 2000 seconds dosing time, the average cluster height is almost identical. For 3600 seconds dosing time the height of the clusters is almost precisely doubled. Also it is noticeable that the height of the nanoclusters agrees with the diameter of a gold atom (0.27 nm ;[12])

Dosing time (seconds)	Cluster width (nm)	Cluster height (nm)
1000	1.7	0.23
2000	2.2	0.24
3600	3.1	0.48

Table 6.1: The width and height of the gold nanoclusters for different dosing times

quite well. Considering all these facts the conclusion is that the gold atoms grow in a 2D island fashion for dosing times of 1000 an 2000 seconds whereas they grow in 3D islands for 3600 seconds dosing time. This also suggests that the total amount of gold atoms on the surface is below one monolayer for 1000 and 2000 seconds dosing time whereas it is above one monolayer for 3600 seconds.

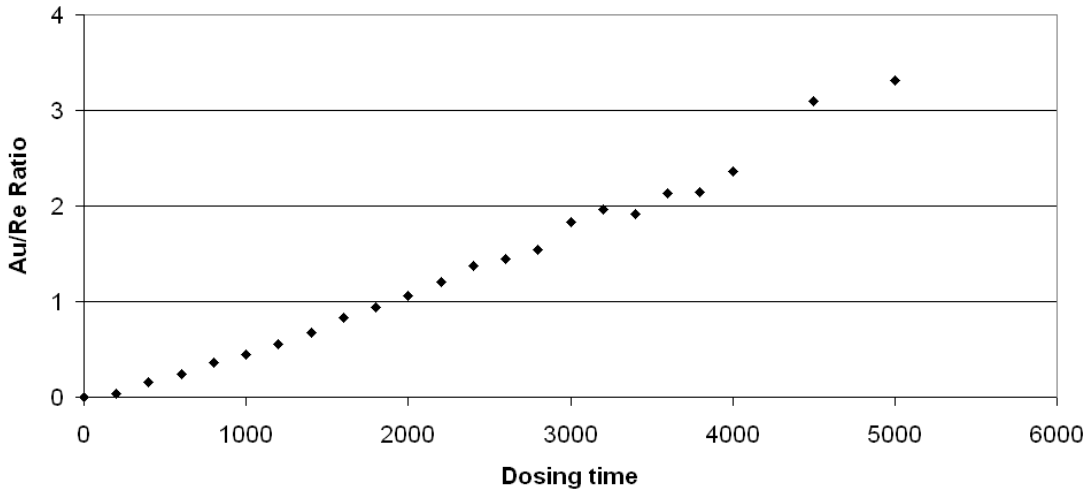

Figure 6.6: Ratio between the gold Auger signal and the rhenium Auger signal as a function of dosing time (in seconds)

The growth of the gold atoms was also observed using Auger electron spectroscopy. In order to understand the growth mode the ratio between the rhenium Auger signal and the gold Auger signal was monitored for different gold doses from 0 to 5000 seconds (Figure: 6.6). A linear dependency was observed between the Re/Au ratio and the dosing time. This linear behavior also leads to the conclusion that the gold atoms grow in the Volmer-Weber growth mode right from the beginning, because some change in the

behavior would be expected for Frank-van der Merwe or Stranski-Krastanov growth due to the full wetting of a surface layer.

In order to obtain a qualitative dependency between the dosing time and the absolute gold coverage an interesting experimental observation was used. It was observed that the gold clusters on top of the Re surface disappear after annealing the surface to temperatures around 870 - 900 K. Instead of building clusters on top of the facets, the gold atoms then wet the surface completely (Figure: 6.7). By a careful analysis of the STM images of the wet surface it is possible to relate the dosing time of gold to an absolute coverage.

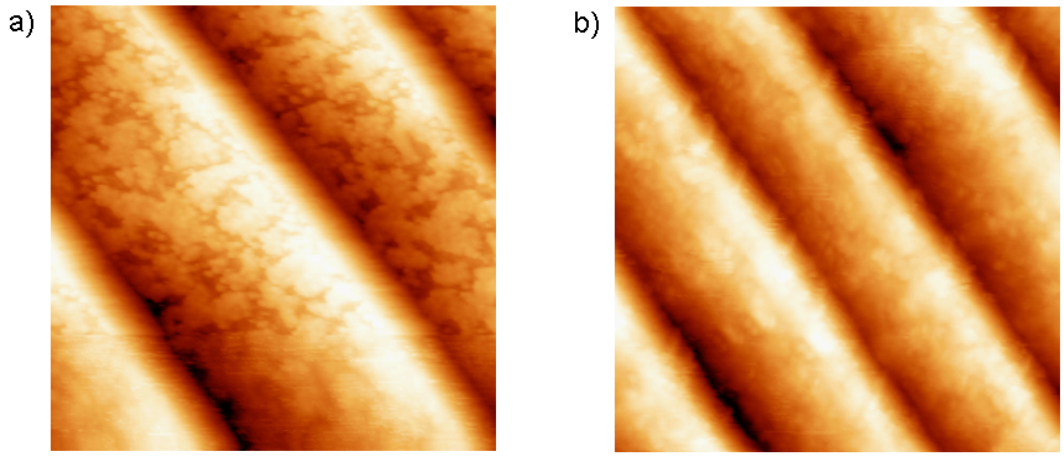

Figure 6.7: STM images (50 nm × 50 nm) of gold covered surface after first annealing to T= 870K - 900K. a) 2000 seconds dosing time ; b) 3600 seconds dosing time

If Fig. 6.7 (a) is examined carefully, some dark areas can be spotted in it. By using the STM line scan tool the depth of this "valleys" was determined. It was found to be around 0.24 nm, which is the same as the height of the clusters found previously to the annealing. So we conclude that the valleys in Fig. 6.7 (a) are uncovered surface areas. Also we can see in Fig. 6.7 (b) that there are no valleys for the 3600 second dose. This implies that the coverage here is more than one monolayer. This observations also agree

with the interpretation of the cluster heights previous to the annealing; 2D islands for 1000 seconds and 2000 seconds dosing time and 3D islands for 3600 seconds dosing time.

By analyzing the area of the valleys in Fig. 6.7 (a) it is possible to determine the gold coverage. Thereby you also have to take account of the fact that the surface area of the faceted surface is larger than that of a planar one (Section: 6.1.1). By considering that, we finally obtain the following relations between dosing time and gold coverage (Table: 6.2). Here a monolayer is defined as the (hypothetical) coverage that would result from a closed-packing of the gold adatoms in a single, complete 2D atomic layer.

Dosing time (seconds)	**Gold coverage θ (monolayer)**
1000	0.4 ± 0.1
2000	0.8 ± 0.1
3600	1.4 ± 0.1

Table 6.2: Dosing time and related gold coverage

The given error in the gold coverage results from the uncertainty in the determination of the uncovered surface areas in Fig. 6.7 (a).

From now on and for the further course of this thesis all information about the used amount of gold will be given in terms of coverage.

6.1.3 Temperature dependence of the morphological change

In this section the morphological change of the gold covered surface structure and its dependency on the annealing temperature of the surface is investigated. Therefore a fixed amount of gold ($\theta = 0.8$ ML) was dosed on the faceted surface. Afterwards the sample was annealed to increasing temperatures in a step-wise fashion. After every step, when the sample was cooled down to room temperature again, the surface structure was imaged by scanning tunneling microscopy. Auger electron spectroscopy was used to assure that gold did not desorb from the surface due to the annealing

Fig. 6.8 shows the faceted Re surface after the dose of 0.8 ML gold on top of it. Gold nanoclusters are clearly visible on the surface[4]. The structure of the original sawtooth ridges is also observed and seems to be unchanged from oxygen-induced facets prior to gold deposition.

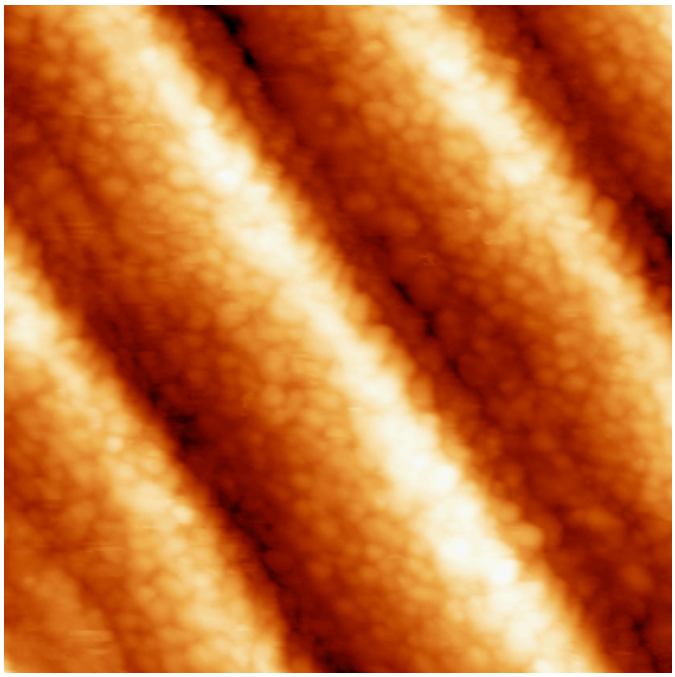

Figure 6.8: 50 nm × 50 nm STM image of the faceted Re surface after the dosing of 0.8 ML gold on top of it. Gold nanoclusters covering the whole surface area are clearly to see in this image.

After annealing the sample for the first time to a temperature around 870 K for 30 minutes, a drastic change in the surface morphology can be observed (Figure: 6.9). The gold nanoclusters are no longer found on top of the facets. Instead, the surface seems to be fully wetted by the gold atoms. The darker areas in the image, which look like valleys, result from the fact that the gold coverage is less than one monolayer and are attributed to uncovered surface areas. These areas disappear if a coverage above one monolayer is used. If one carefully studies the image it is possible see that there is no

[4]more details about the gold nanoclusters in section 6.1.2

gold film on top of the $(01\bar{1}0)$ facet. Rather you can sense atomic rods on this side, which belong to the original facet structure. The original two sided ridges still seem to be well defined and unchanged.

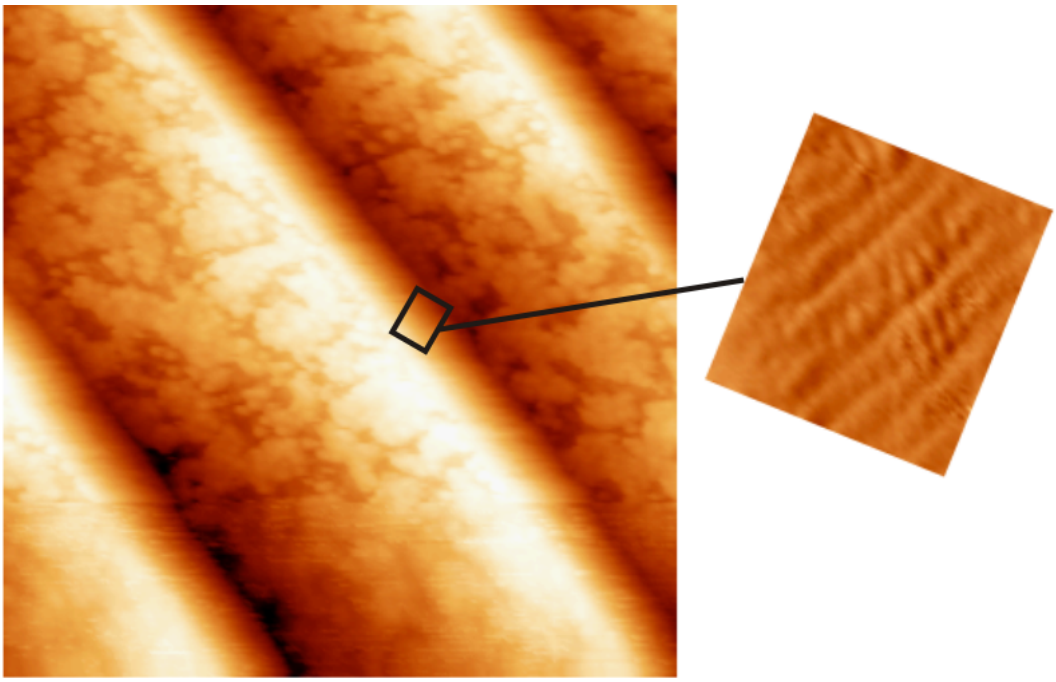

Figure 6.9: 50 nm × 50 nm STM image of the gold covered ($\theta = 0.8$ ML) faceted Re surface after the first annealing to 870 K for around 30 minutes. It is clearly to see that the gold is wetting the surface. The dark areas are attributed to uncovered surface areas. The enlarged cut-out shows the atomic row structure of the $(01\bar{1}0)$ facet.

After the second annealing of the sample, which went to a temperature of around 930 K for 30 minutes, another fundamental change in the structure of the two sided ridges is observed (Figure: 6.10). The sawtooth structure is gone and instead of it there are arrays of small triangular "pyramid" on top of the surface. These pyramids are arranged in lines that have the same orientation as the original sawtooth ridges. All pyramids seem to have a similar size and a uniform orientation. They appear to be composed of three single facets. An interesting feature of this new surface structure is that the $(01\bar{1}0)$ facets of the original ridges still seem to be intact; it is still possible to sense atomic

rods on it. Thus it is suspected that the pyramid structure develops due to the formation of two new facet sides out of the original $(11\bar{2}1)$ facet. More detailed information about these pyramidal structure is given in section 6.1.5. Finally it also should be mentioned that the different size of the original ridges in Fig. 6.10 is due to the procedure of making the original facets. The size of the ridges does not change due to the annealing.

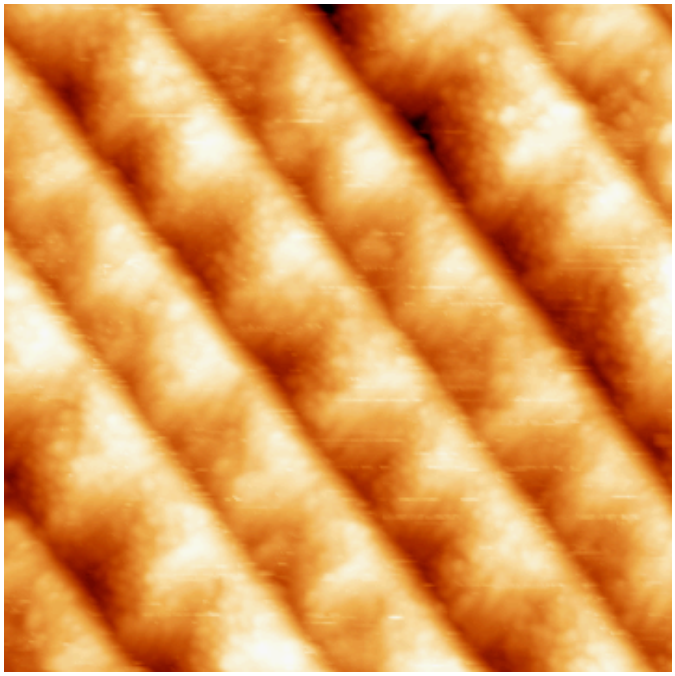

Figure 6.10: 50 nm × 50 nm STM image of the gold covered (θ = 0.8 ML) faceted Re surface after the second annealing to temperatures around 930 K for 30 minutes. The original sawtooth structure of the facets is gone and instead of it a structure consisting of "three sided pyramids" has developed on the surface.

After another annealing of the pyramidal structure to a higher temperature of around 970 K for another 30 minutes, the morphology of the surface changed again. Now the original sawtooth structure finally disappeared completely and a totally new structure evolved. This new structure also looks like two sided ridges, but the direction of the ridges seems to be rotated by approximately 90°. Also the facets appear not to be fully developed. They do not have a sharply defined structure, but look more like a structure

in the progress of evolution. As will be shown in section 6.2, this structure develops due to the destruction of the oxygen induced ridges. We will find out that these ridges have the same structure as gold induced ridges that developed on a planar Re $(12\bar{3}1)$ surface after annealing.

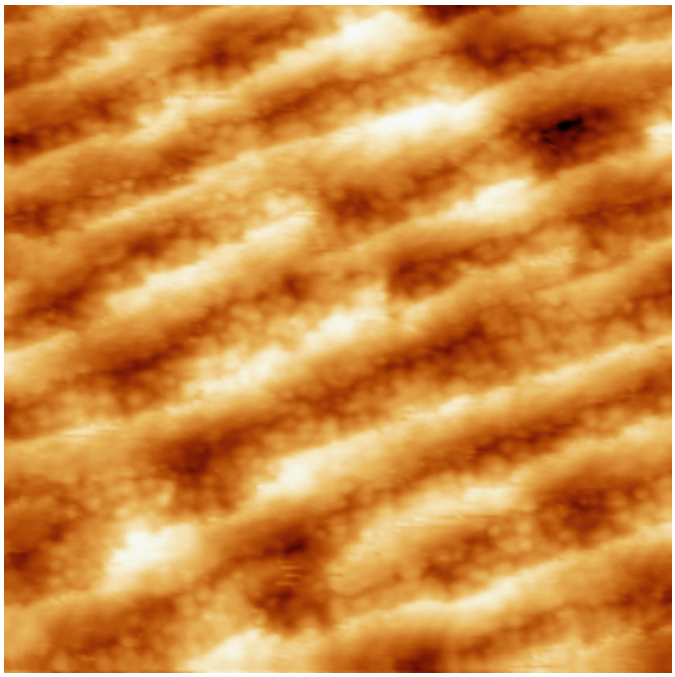

Figure 6.11: 50 nm × 50 nm STM image of the gold covered (θ = 0.8 ML) faceted Re surface after the third annealing to temperatures around 970 K for 30 minutes. As you can see the surface structure changed completely. The oxygen induced ridges disappeared totally and instead of that new underdeveloped two sided ridges with the orientation turned by around 90 ° emerged.

Further annealing of the sample to higher temperatures did not show any evidence for new surface structures. Finally, after annealing to temperatures above 1200 K, all surface structures were destroyed and gold was desorbed from the surface.

It is worth mentioning that the same evolution of the surface morphology due to annealing was also found for coverages different from 0.8 ML. There might be slight changes in annealing temperatures and times due to the change in coverage, but the general evolution keeps the same.

Conclusions:

The originally gold covered (θ = 0.8 ML) faceted Re surface underwent a huge morphological evolution after consecutive annealing of the sample to different temperatures. First the surface became smoother and the gold atoms started wetting the surface. Further annealing lead to the development of a "pyramidal" structure. Finally, after another annealing, the pyramids also disappeared and a new structure showing underdeveloped two sided ridges, that are turned by around 90° with respect to the original ridges, emerged.

This evolution of the surface morphology suggests that gold has the ability to induce new facets on the faceted rhenium surface. The fact that the $(01\bar{1}0)$ facet is still existing in the pyramidal structure indicates that the new facets that appear to form the pyramidal structure emerge on the $(11\bar{2}1)$ facet side. Therefore it is suspected that gold also has the capability to induce faceting on a planar Re $(11\bar{2}1)$ surface.

6.1.4 Coverage dependence of the morphological change

In this section the coverage dependency of the morphological change is investigated. Indeed the general morphological evolution observed in section 6.1.3 is the same for different coverages, but there is one distinctive difference in the morphological change; the development of the "pyramidal" structure depends on the gold coverage of the faceted Re surface.

To study the development of the pyramids in dependency of the gold coverage three different gold coverages of 0.4 ML, 0.8 ML and and 1.4 ML were dosed on the faceted Re template. Afterwards, the gold covered surfaces were annealed stepwise, whereby the quality of the surface structure was checked by scanning tunneling microscopy, until the pyramid structure was as well developed as possible. STM images and x-slope[5] STM images of the obtained pyramidal structure for all three coverages are given in Fig. 6.12.

[5]Processing mode for STM images; thereby the derivative of the height in x-direction is taken.

In the Fig. 6.12 (a) the pyramidal structure for a gold dose of 0.4 ML is shown. It is clearly to see that a pyramid consists of three different facets. The different size of the single pyramids is due to the original sawtooth ridged structure, which was not as uniformly developed as it normally was. If one examines Fig. 6.12 (a) carefully it can be seen that the size of one of the facets is much smaller than the size of the other facets. Also, one can see that the same facet is much better developed for 0.8 ML coverage, as shown in Fig. 6.12 (b), too. This leads to the conclusion that this facet does not fully develop for a coverage of 0.4 ML.

Another interesting feature in Fig. 6.12 (a) are the small dots on top of the biggest facet. These dots are single atoms. By studying their arrangement more carefully it is possible to get information about the atomic structure of this facet (Section: 6.1.5).

Fig. 6.12 (b) shows the pyramidal structure for a coverage of 0.8 ML. All three facets are clearly visible and well defined. In Fig. 6.12 (b2) it is clearly to see that one facet, $(01\bar{1}0)$, stretches out all over the image without interruption. This affirms the assumption that the pyramid structure develops due to the appearance of two new facets on top of the $(11\bar{2}1)$ facet, whereas the $(01\bar{1}0)$ facet remains unchanged.

In Fig. 6.12 (c) the pyramidal structure for a coverage of 1.4 ML can be seen. All three facets are clearly visible. But the structure of the facets is not as sharp and well defined as it was for both of the lower coverages. It looks more like the facets are slightly destroyed. It is believed that this is due to the fact that the annealing temperature needed in order to develop the pyramid structure increases with the gold coverage. The temperature needed to get fully developed pyramids for a coverage of 1.4 ML is higher than the temperature at which the destruction of the original oxygen induced facets starts. This explains why the facets look a little bit destroyed.

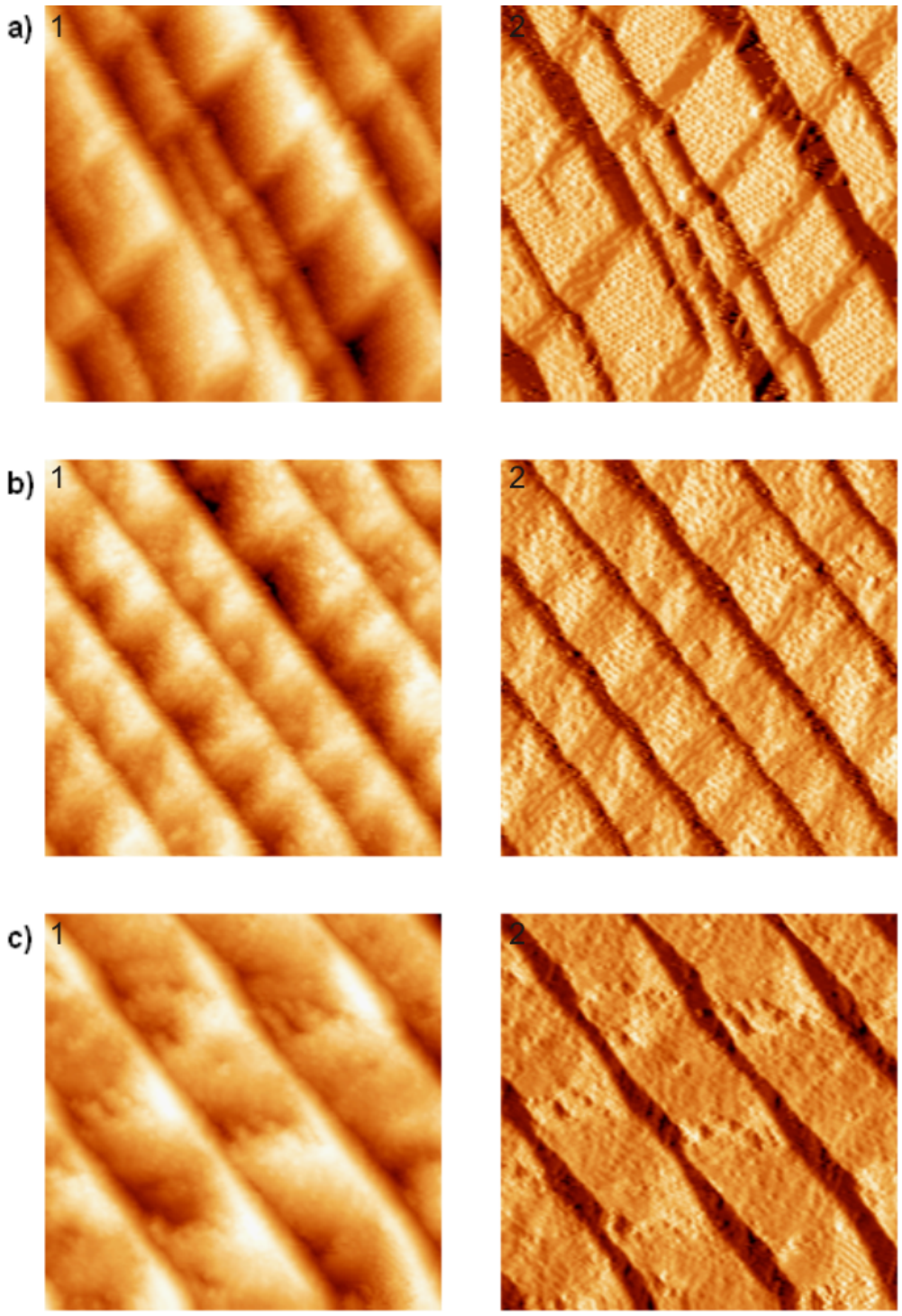

Figure 6.12: 50 nm × 50 nm STM (1)/x-slope STM (2) images of the pyramidal structures for different gold coverages. a) $\theta = 0.4$ ML ; b) $\theta = 0.8$ ML ; c) $\theta = 1.4$ ML

Conclusions:

It was found that for a gold coverage of 0.4 ML one of the pyramid facets is not fully developed. Therefore it is believed that there is a minimum gold coverage that is required in order to fully develop the pyramidal structure. Since for 0.8 ML gold coverage the pyramids seem to be fully developed the minimum coverage should be located between 0.4 ML and 0.8 ML.

Also it has been observed that the facet structure for 1.4 ML coverage is not as sharp and well defined as it is for the lower coverages. This is attributed to the fact that the mass transport that is required to form fully developed facets increases with the coverage. In order to enhance the mass transport, a higher annealing temperature is necessary. It is believed that for a gold coverage of 1.4 ML the necessary annealing temperature is higher than the temperature at which the destruction of the original oxygen induced facets starts. Therefore the facet structure for 1.4 ML coverage looks not as sharp and well defined.

A possible solution to get well developed facets for higher coverages might be to increase the annealing time instead of the temperature, which may achieve a sufficient mass transport without destruction of the oxygen induced facets.

6.1.5 Gold induced three sided pyramids

In this section, the pyramidal structure that was found in the previous sections after annealing the gold covered oxygen induced ridges, is investigated more detailed. The general shape of the structure and its arrangement is discussed. Also the orientation of the pyramids facet and their atomic structure is examined in this section.

The Fig. 6.13 (a) and (b) both show 50 nm x 50 nm 3 dimensional renderings of the pyramidal structure shown in Fig. 6.10. Fig. 6.13 (a) shows the front side of the pyramidal structure with two of the facets visible. Fig. 6.13 (b) is rotated by around 180° with respect to Fig. 6.13 (a), so that the third facet is visible.

In Fig. 6.13 (a) the structure of the pyramids is clearly to recognize. They are arranged uniformly along the $[\bar{2}113]$ direction of the original oxygen induced ridges. Also the shape and size of the pyramids is quite uniform. In Fig. 6.13 (b) it is clear that one facet is uninterrupted for all the pyramids along one line in the $[\bar{2}113]$ direction. This confirms that this facet remains from the original sawtooth ridges structure. Also atomic rows can be found on this facet, which identifies the orientation of this facet as $(01\bar{1}0)$.

Fig. 6.13 (c) shows a 25 nm × 25 nm STM image of the pyramidal structure. The black line indicates the direction of the line profile which is shown in Fig. 6.13 (e). The line profile is taken at half way between two $(01\bar{1}0)$ facets and in $[\bar{2}113]$ direction. It clearly shows that the original $(11\bar{2}1)$ facet of the sawtooth ridges is gone and instead two new facets have developed on it. The figure also shows that the pyramidal structure is well defined and several atoms high.

Fig. 6.13 (d) shows the same image as Fig. 6.13 (c), only the derivative in the x-direction is taken now. Thereby all three facets of the pyramid structure become clearly visible. So it is possible to realize that the size of the both facets that developed on the original $(11\bar{2}1)$ facet are almost equal in area.

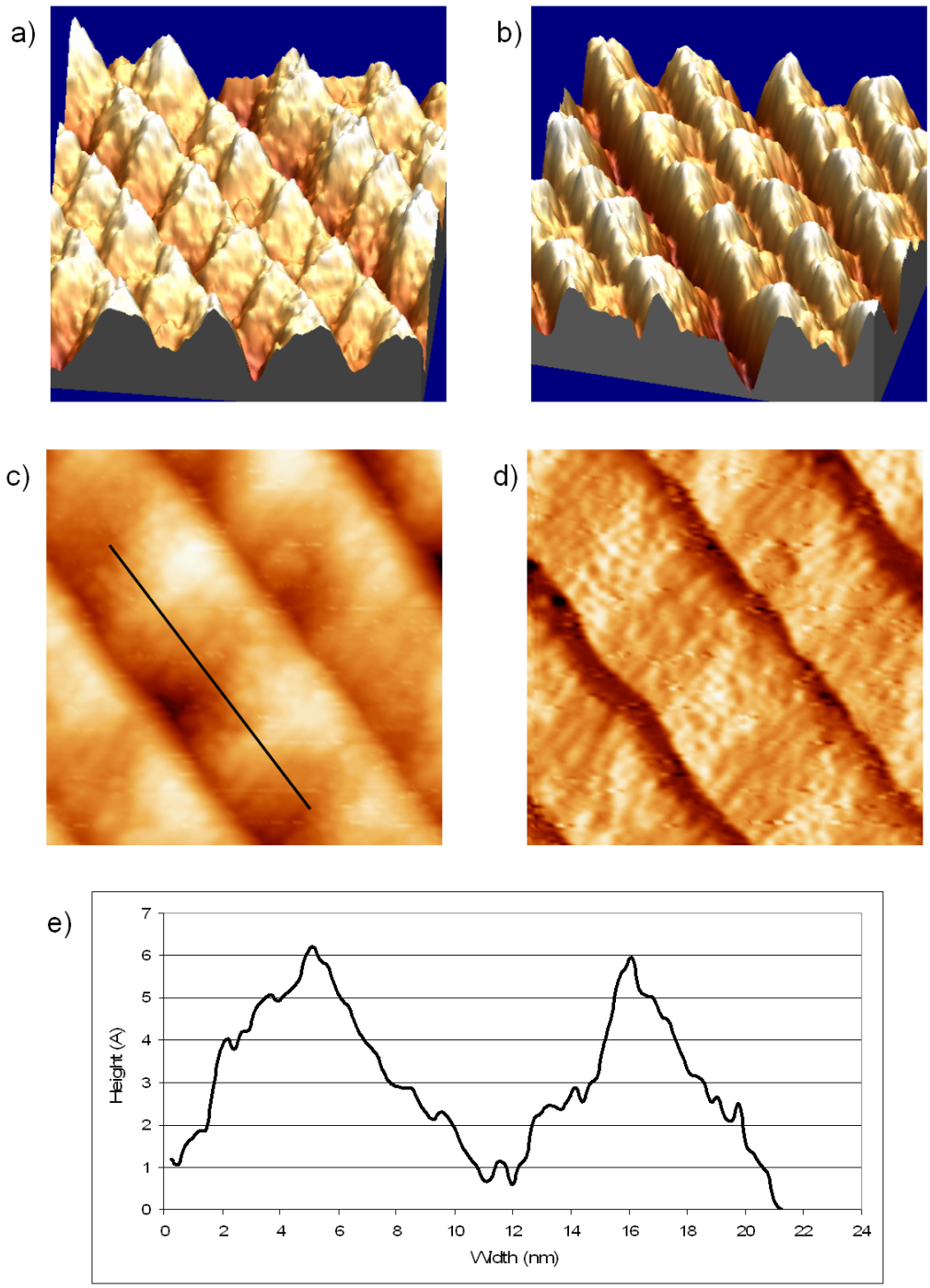

Figure 6.13: The Fig. 6.13 (a) and (b) both show a 50 nm × 50 nm 3 dimensional rendering of the pyramidal structure shown in Fig: 6.10 ; c) 25 nm × 25 nm STM image of the pyramidal structure. The black line indicates the direction of the line profile in e) ;
d) 25 nm × 25 nm x slope image of c) ; e) Line profile as indicated in image c)

Orientation of the pyramid's facets

In this section we try to work out the orientations of the three facets that comprise the pyramidal structure. To accomplish this, LEED experiments were performed on a fully developed pyramid structured surface (0.8 ML gold coverage). Also tilt angle calculations were applied to identify the surface structure (Table: 6.3).

The LEED images (Figure: 6.14) showed three sets of spots moving in different directions. One set of spots was very bright and sharp, whereas both the other sets were weak and blurry. The bright spots all moved towards a specular beam position outside the LEED-screen, as indicated in Fig. 6.14 (a) by yellow arrows. This motion agreed with the motion of the $(01\bar{1}0)$ spots that was found for the two sided ridges in section 6.1.1. The location of the specular beam, outside the screen, also agrees with tilt-angle calculations; the tilt-angle between $(12\bar{3}1)$ and $(01\bar{1}0)$ is too large to find the $(01\bar{1}0)$ spectral beam on the LEED screen (Table: 6.3). Consequentely, the bright spots were assigned to the $(01\bar{1}0)$ facet orientation. This also agrees with STM images, which show that the $(01\bar{1}0)$ facet of the original two sided ridges remains as one of the pyramidal facets.

The second set of spots corresponds to the $(11\bar{2}0)$ orientation. For this spots the specular beam was found on the screen. The facet orientation was identified by analysis of the position of the spectral beam. The tilt angle between the $(11\bar{2}0)$ plane and the $(12\bar{3}1)$ substrate was calculated as 15.3° from the LEED images. Considering the possible errors for the LEED measurements (position of the camera, detecting the spectral beam precisely, etc.), this agrees well with the theoretical value of 16.4°. Also the position of the spectral beam on the screen agreed well with the expected spectral beam position for the $(11\bar{2}0)$ orientation (Figure: 6.14 b).

The third set of spots was identified as $(11\bar{2}1)$. This is the orientation of the second facet of the original two sided ridges (besides $(01\bar{1}0)$). It is not possible to form three sided pyramids with $(01\bar{1}0)$, $(11\bar{2}0)$ and $(11\bar{2}1)$ facets on a $(12\bar{3}1)$ substrate geometrically.

Also there is no evidence in the STM images that this facet occurs as one of the pyramids side. Thus the appearance of this set of LEED spots is attributed to the fact that the pyramid structure was not fully developed all over the surface during the LEED measurement and there were areas left with two sided ridges structure.

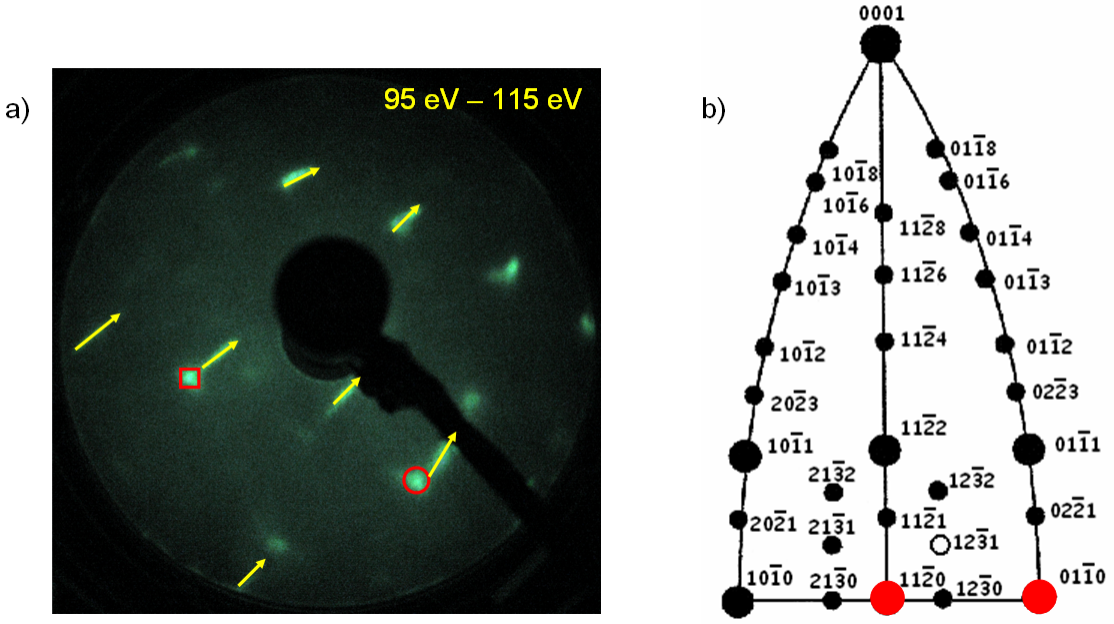

Figure 6.14: a) LEED image of the pyramid surface structure. The direction of motion for the $(01\bar{1}0)$ spots is marked with arrows. The spectral beams of the $(11\bar{2}1)$ and$(11\bar{2}0)$ facets are marked by a red circle/ square. The motion of their spots is not visible here, due to the low brightness of the spots. (Electron energy: 95 eV - 115 eV)
b) Stereographic projection of the hcp lattice. The two facets of the pyramids found in the LEED image are marked by a red dot.

Since we did not get any information about the third facet orientation out of LEED analysis, we need to use a different method to identify their orientation. Considering the stereographic projection in Fig. 6.14 (b) there are not so many stable surfaces left as possible third facets. $(11\bar{2}2)$, $(12\bar{3}2)$, $(01\bar{1}1)$ and $(02\bar{2}1)$ are the only orientations left in the vicinity of $(12\bar{3}1)$, which can be considered as the third facet.

Remembering the fact that the third facet emerged on the original $(11\bar{2}1)$ facet, $(01\bar{1}1)$ and $(02\bar{2}1)$ can be excluded as a possible facet, since these facets have a too large

tilt angle with respect to the $(11\bar{2}1)$ orientation. Furthermore their orientation does not agree with the pyramidal structure seen in the STM images.

The STM images also suggest strongly that the $(01\bar{1}0)$ facet has the largest tilt angle of all facets with the planar $(12\bar{3}1)$ orientation. Hence it is also possible to also exclude $(11\bar{2}2)$ orientation, since its tilt angle with $(12\bar{3}1)$ is bigger than that for $(01\bar{1}0)$ (Table: 6.3). Consequently there is only the $(12\bar{3}2)$ orientation left as a possible facet; it was possible to determine the third facets orientation by the process of elimination.

Surface orientation	**Tilt angle with respect to** $(12\bar{3}1)$
$(11\bar{2}1)$	12.2
$(01\bar{1}0)$	22.6
$(11\bar{2}0)$	16.4
$(12\bar{3}2)$	11.3
$(11\bar{2}2)$	23.6
$(01\bar{1}1)$	25.0
$(02\bar{2}1)$	18.9

Table 6.3: Tilt angle between selected hcp surface orientations with respect to $(12\bar{3}1)$.

One question that occurs is why we did not see the third spectral beam on the LEED screen. According to the tilt angle calculations we should be able to see it. This is probably also due to the fact that the pyramids structure was not defined well enough as was observed in the STM measurements. Therefore this spectral beam was to weak to see.

Conclusions

In this section the orientation of the pyramids facet were analyzed. By means of low energy electron diffraction and tilt angle calculations it was possible to determine the orientations of the pyramid's facets. The three facets were determined as $(01\bar{1}0)$, $(11\bar{2}0)$ and $(12\bar{3}2)$ orientations.

Atomic structure of the pyramids facets

By analyzing atomically resolved STM images of the surface structure it is possible to get information about the atomic arrangement of the pyramids facets. It was possible to obtain atomically resolved images of two of the pyramids facet. Fig. 6.15 shows a 25 nm × 25 nm x-slope STM image of a pyramid structured surface. In this image all three facets of the pyramidal structure are clearly to see. They are marked with numbers from (1) to (3). The image was taken on a surface with 0.4 ML gold coverage; this is why one of the pyramids facets (3) is underdeveloped (Section: 6.1.4). The orientation of the facets was determined in the previous section as $(12\bar{3}2)$ for (1), $(01\bar{1}0)$ for (2) and $(11\bar{2}0)$ for (3).

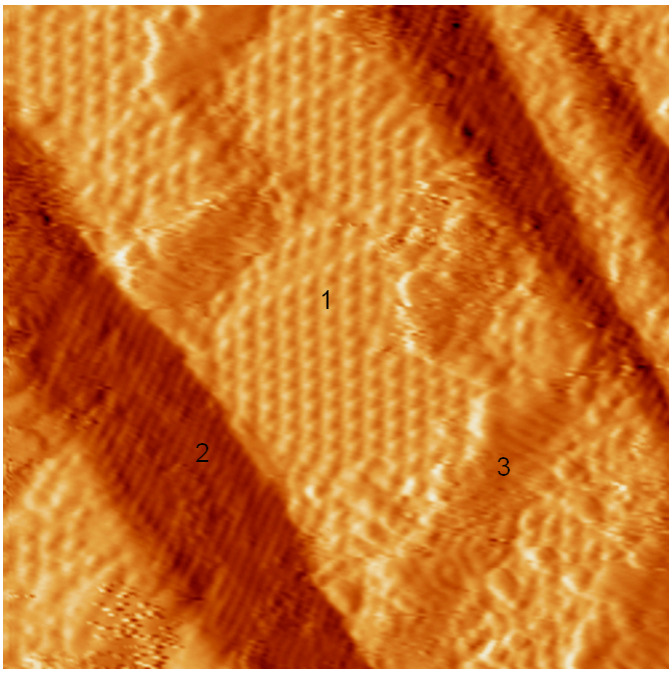

Figure 6.15: 25 nm × 25 nm x-slope STM image of a pyramid structured surface. The numbers (1-3) indicate the three different facets of the pyramids structure.

Fig. 6.16 (a) shows a 4.1 nm × 4.7 nm STM image of the facet (1) in Fig. 6.15. From this image you can clearly see the atomic structure of this facet. It looks like a

honeycomb structure, which is compressed a little bit in one direction. In Fig. 6.16 (b) a graphic of the atomic structure in Fig. 6.16 (a) is shown and all spacings are given. You can also interpret the structure of this facet as a zig-zag-chain structure. This interpretation is indicated in Fig. 6.16 (b) with a black line.

Since the atomic structure shown in Fig. 6.16 (a) does not match the atomic structure of the $(12\bar{3}2)$ hcp lattice it is believed that there is an overlayer of gold atoms on this facet. Due to lattice strains the gold atoms rearranged themselves in a way which better fits their own fcc bulk structure and thereby created the atomic structure shown in Fig. 6.16. Therefore it might be also possible that this surface structure changes with gold coverage.

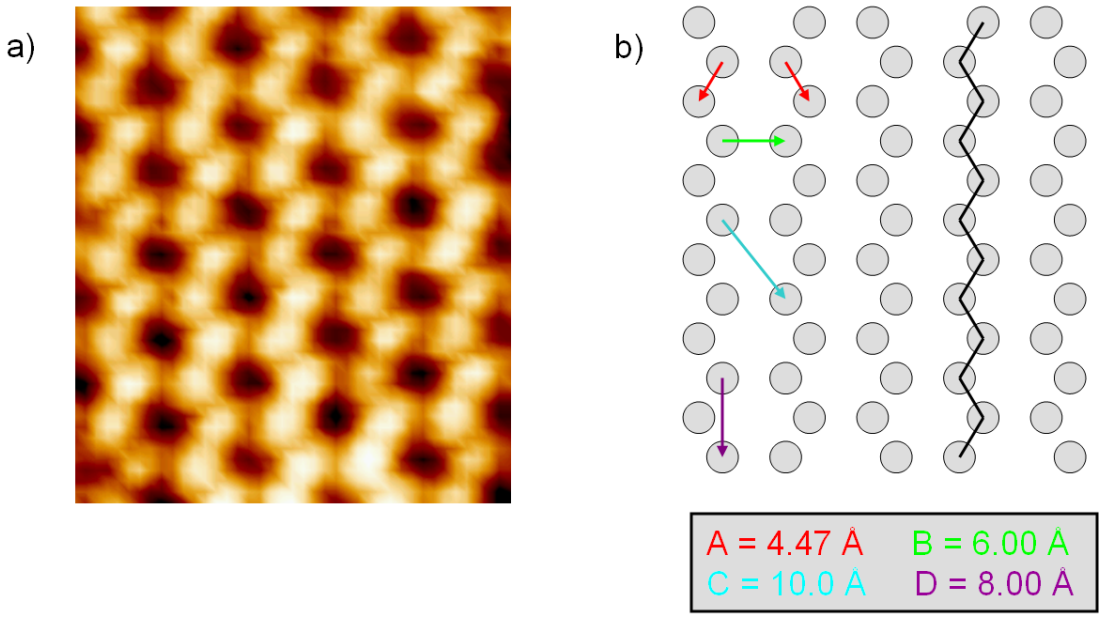

Figure 6.16: a) 4.1 nm × 4.7 nm STM image of the (1) facet of the pyramids structure in Fig. 6.15). You can clearly see the quasi-honeycomb atomic structure of this facet.
b) Graphics of the atomic structure in a); Atomic spacings as indicated by arrows.

Fig. 6.17 (a) shows a 8.8 nm × 9.9 nm STM image of the facet (2). The atomic structure of the facet is clearly visible. It consists of close-packed atomic rows. This structure agrees with the atomic structure of the hcp $(01\bar{1}0)$ orientation, which also shows atomic close-packed rows (Figure: 6.17 b). The theoretical distance between two

of the close-packed rows for the $(01\bar{1}0)$ orientation is 5.17 Å. The distance between two atomic rows in Fig. 6.17 (a) was determined experimentally as 4.2 Å ± 0.4 Å. This experimental value is similar to the theoretical value, but does not agree with it within the error of the measurement. However, within this error there are only uncertainties of measurement itself considered. Errors due to the procedure of taking the image (shape of the tip, etc.) are not considered and may increase the total error, so that it is likely that the experimental and theoretical value agree within the total error.

Therefore it is believed that facet (2) shows the unchanged Re $(01\bar{1}0)$ surface structure without any gold overlayer on top of it.

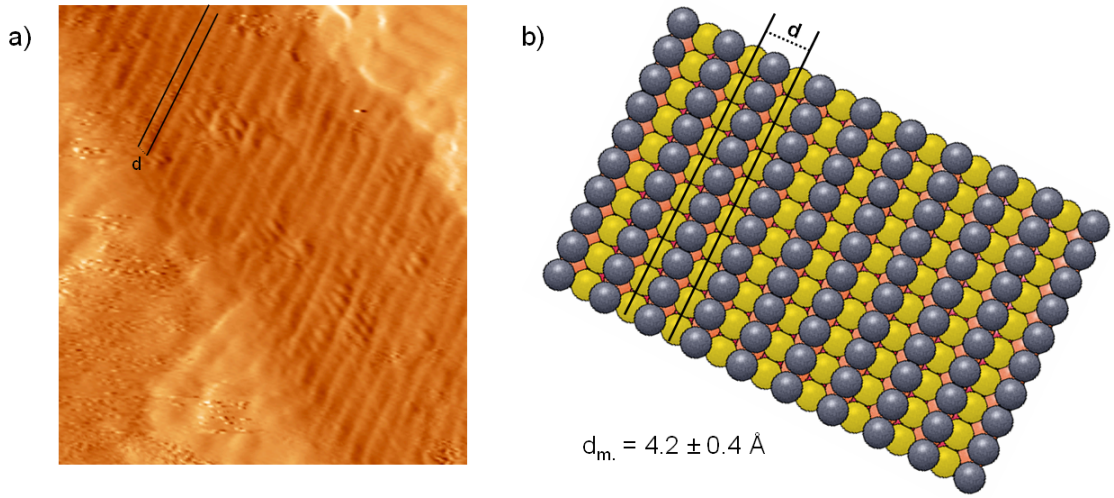

Figure 6.17: a) 8.8 nm × 9.9 nm STM x-slope image of the second facets of the pyramids structure. You can clearly see the closed packed atomic row structure of the $(01\bar{1}0)$ orientation. b) Hard sphere model of the hcp $(01\bar{1}0)$ orientation. The distance (d), measured between two atomic rows in a), is indicated.

As can be seen in Fig. 6.15, the third of the pyramidal facets also shows some kind of atomic row structure. Unfortunately it was not possible to obtain atomically resolved images of it. So it is not possible to analyze this surface structure in more detail.

6.1.6 Controlling the size of the pyramids

As was shown in the previous sections it is possible to create a triangular pyramidal structure on our rhenium surface. Since oxygen induced sawtooth ridges are used as a template in order to develop this pyramids, it might be possible that the size of these ridges is correlated to the size of the pyramidal structure. This consideration is also supported by the fact that the $(01\bar{1}0)$ facet of the original ridges remains as one of the pyramidal facets. If there is a correlation between the size of the oxygen induced facets and the pyramids size this can be used to control the size of the pyramids, as the size controll of the oxygen induced facets is well understood [24].

In Fig. 6.18 (a) and (b) you can see two STM images of the pyramidal structures. Both of the images were obtained in the same process of dosing gold and annealing the surface. The only difference is that the images were taken at entirely different areas of the surface.

It is clear that the size of the pyramids in Fig. 6.18 (a) is much smaller than the size of the pyramids in Fig. 6.18 (b). It also seems that the original oxygen induced facets were much smaller in Fig. 6.18 (a) than in Fig. 6.18 (b). In order to confirm this suspicion, the average width of both the pyramids and the original sawtooth ridges was determined with the STM line profile tool. Thereby the width of a pyramid (p) was defined as the normal distance from the pyramids $(01\bar{1}0)$ facet to the opposite edge of the pyramid, whereas the pyramid was mapped on the $(12\bar{3}1)$ plane (Figure: 6.18 c). The width of the original two sided ridges (w) was defined as the peak to peak distance between two of the remaining $(01\bar{1}0)$ facets (Figure: 6.18 c).

Figure: 6.18	**Pyramid width p (nm)**	**Width of ridges w (nm)**
(a)	9.9	10.7
(b)	20.9	22.0

Table 6.4: Average width of both the pyramids and the original two sided facets in Fig. 6.18 (a) and (b).

Indeed, the measurements confirmed the suspicion. The width of the original ridges in Fig. 6.18 (a) is much smaller than that in Fig. 6.18 (b) (Table: 6.4). This means the width of the pyramids and consequently the total size of the pyramids is correlated to the width of the original facets.

Another confirmation of this correlation is given in Fig. 6.18 (d). It shows the height profile of one pyramid. If one compares this profile with the height profile of the original ridges (Figure: 6.2) it possible to realize the similarities of both of the height profiles, which also indicates the width correlation.

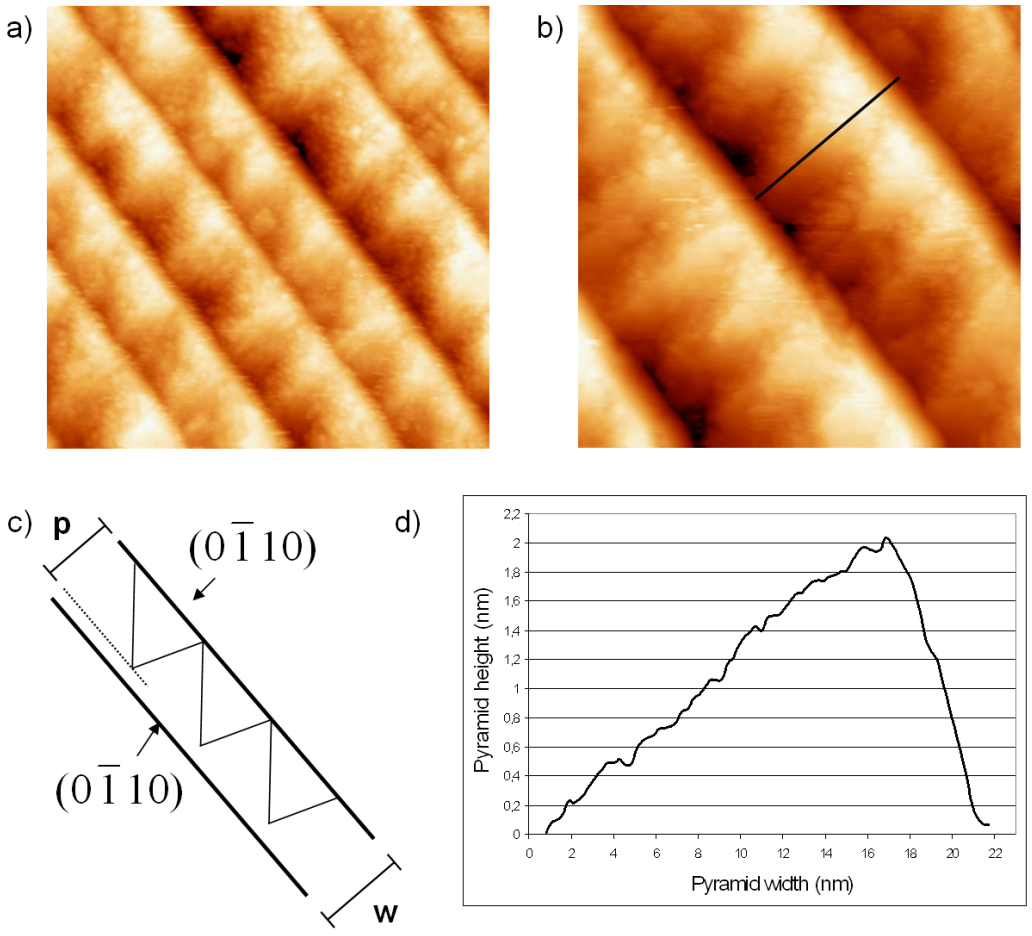

Figure 6.18: a) and b): 50 nm × 50 nm STM images of pyramidal structures on the Re substrate ; c) Definition of the pyramids width (p) and the width of the original two sided ridges (w) ; d) Height profile of one of the pyramids in b) (as indicated by black line).

Conclusions:

The existence of a clear correlation between the size of the pyramids and the size of the two sided oxygen induced ridges was shown. The size of the pyramids increases with the size of the sawtooth ridges.

This dependency can be used to control the size of the pyramids, since the size control of the oxygen induced facets is well understood. A variation in the annealing temperature or annealing time during the creation of the two sided ridges will result in a variation of the ridges size [24].

6.2 Gold induced faceting on a planar Re $(12\bar{3}1)$ substrate

In the last section we saw that dosing gold on a faceted Re $(12\bar{3}1)$ surface followed by annealing of the surface drastically changed the morphology of the surface. The results suggested that gold has the ability to induce new kind of facets on the oxygen induced faceted surface.

In this section we want to examine if gold also has the ability to induce faceting on a planar Re $(12\bar{3}1)$ surface. Therefore 0.8 ML of gold was deposited on the planar Re $(12\bar{3}1)$ surface. Afterwards the crystal was annealed stepwise and the surface structure was checked by STM after every annealing-step.

After the third step where the annealing was to a temperature around 970 K, a change in the surface morphology was found. The surface structure changed from the former planar surface to a surface structure showing two sided ridges (Figure: 6.19).

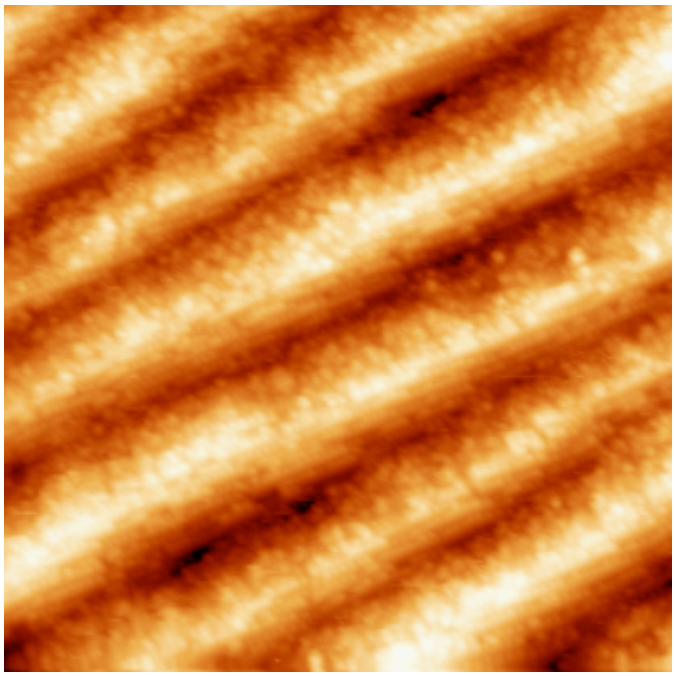

Figure 6.19: 50 nm × 50 nm STM image of the gold induced faceted surface. You can clearly see the surface structure consisting of two sided ridges.

These gold induced ridges were well defined and had a long range order. By using the STM software's line profile tool the dimensions of the ridges were measured. Their average width was around 10 nm and their average height was around 6 Å (Figure: 6.20).

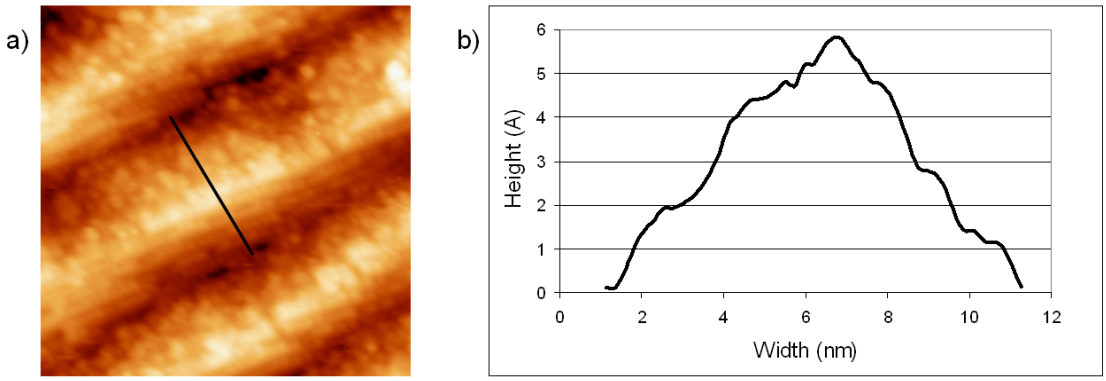

Figure 6.20: a) 25 nm × 25 nm STM image of the gold induced faceted surface.
b) Line profile of a facet in a) as indicated by the black line.

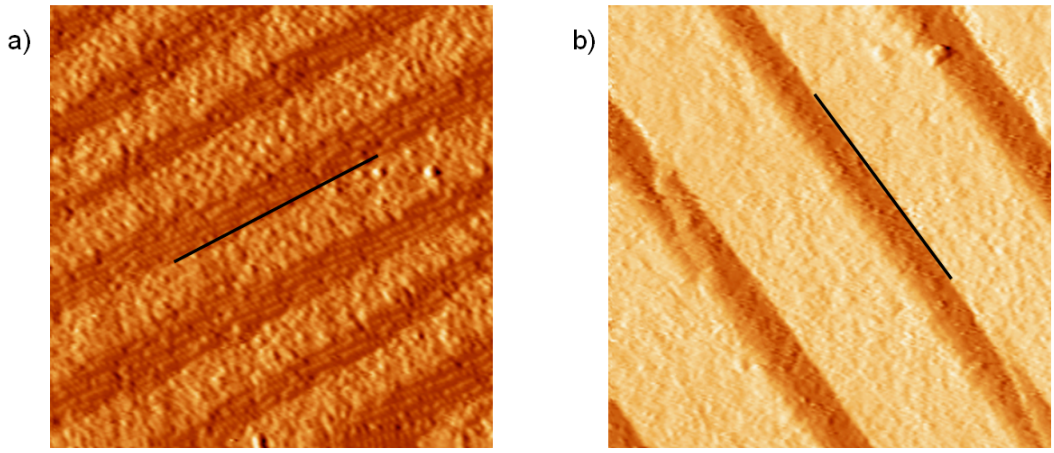

Figure 6.21: a) 50 nm × 50 nm x-slope STM image of the Gold induced two sided ridges on Re $(12\bar{3}1)$. The black line indicates the direction of the facets.
b) 50 nm × 50 nm x-slope STM image of the Oxygen induced facets on Re $(12\bar{3}1)$.

If one compares the newly found gold induced ridges with the oxygen induced ridges of section 6.1 it is possible to realize that both surface structures are entirely different (Figure: 6.21). While the oxygen induced facets are quiet uniform and sharp defined,

the gold induced facets look more ill-defined and less uniform. Also the orientation of both structures is totally different. Both structures are rotated by approximately 90° with respect to each other (Figure: 6.21).

Considering the two sided ridge structure of the facets and the rotation of 90° it is possible to determine the orientation of the gold induced facets. The stereographic projection of the stable surfaces (Figure: 6.22) shows that there are only two possibilities for the two sided ridges. $(11\bar{2}0)/(01\bar{1}1)$ or $(12\bar{3}0)/(12\bar{3}2)$ are the only combinations that can form two sided ridges on a $(12\bar{3}1)$ substrate and are also rotated approximately 90° with respect to the oxygen induced ridges.

The projection also shows that the tilt angle with respect to the $(12\bar{3}1)$ orientation is very different for the $(11\bar{2}0)$ and $(01\bar{1}1)$ facets. The STM images of the gold induced ridges do not suggest that this is the case for the real facets, as you can see in Fig. 6.21 (a). Therefore the most likely orientations for the two sided ridges are $(12\bar{3}0)$ and $(12\bar{3}2)$.

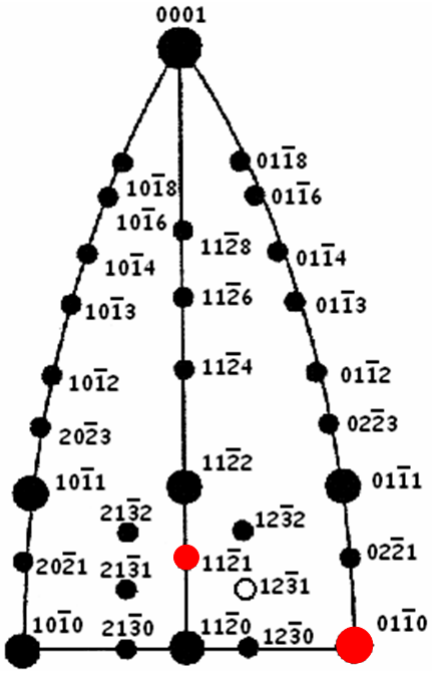

Figure 6.22: Stereographic projection of the hcp lattice. Both of the facets for the oxygen induced ridges are marked with a red dot.

Finally, with the help of the results in this section, we are able to better understand some result from section 6.1.3. There it was found that, after annealing the gold covered oxygen induced ridges for several times to different temperatures, finally a new surface structure also consisting of two sided ridges appeared (Figure: 6.11). The comparison of this surface structure to the structure of the gold induced ridges found in this section displays a distinct similarity between both of the structures (Figure: 6.23).

Therefore it is believed that Fig. 6.23 (a) also shows some gold induced facets. Probably the original oxygen induced facets, on which the gold was dosed in section 6.1.3, were destroyed due to the annealing process. What was left was a planar gold covered Re (12$\bar{3}$1) surface, on which new two sided ridges could be induced by annealing.

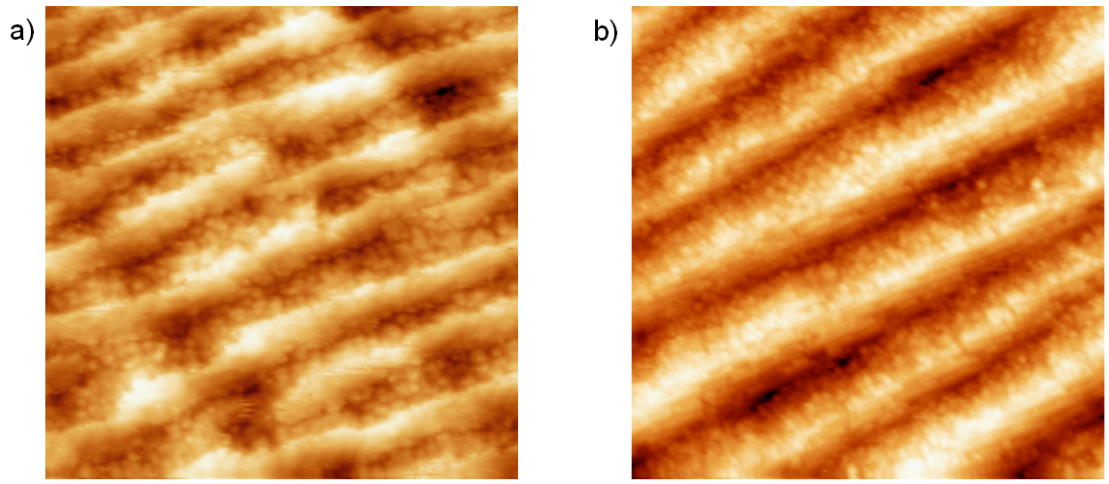

Figure 6.23: a) Surface structure obtained in section 6.1.3 after annealing the gold covered oxygen induced ridges for several times. b) Gold induced facets on the planar Re (12$\bar{3}$1) surface, as shown in this section.

Conclusions:

In this section it was shown that gold induced faceting on a planar Re (12$\bar{3}$1) surface is possible. After dosing 0.8 ML gold on the planar surface and annealing it to temperatures around 970 K a new, gold induced surface structure consisting of two sided ridges

emerged. The ridges had an average width of around 10 nm and an average height of 6 Å. The structure of this ridges was not as uniform as it was for the oxygen induced ridges. Also they were rotated by 90 ° with respect to the oxygen induced ridges. The orientation for both of the ridges facets was determined to be $(12\bar{3}0)$ and $(12\bar{3}2)$.

With this results it is also possible to explain an experimental result obtained in section 6.1.3. After annealing gold covered oxygen induced ridges for several times to different temperatures a new surface structure also consisting of two sided ridges was found there. This structure has a distinct similarity to the the gold induced facets found in this section. Probably the original oxygen induced ridges were finally destroyed in this experiment due to the annealing. Therefore a gold covered planar surface remained, on which new gold induced facets were created.

This also suggests that the onset temperature for oxygen desorption from the faceted Re surface is lower than the temperature at which Au starts to desorb from the surface.

Chapter 7

Conclusion

In this thesis the consequences of depositing a small amount of gold (0.4 ML - 1.4 ML) on a faceted rhenium template were studied. The templates structure consisted of oxygen induced two sided ridges with $(11\bar{2}1)$ and $(01\bar{1}0)$ facet orientations on a Re $(12\bar{3}1)$ substrate.

The effect of dosing 0.8 monolayer of gold on a planar Re $(12\bar{3}1)$ surface was examined as well.

It was found that on top of the faceted rhenium template gold grows in the Volmer-Weber growth mode right from the beginning. For coverages of 0.4 ML and 0.8 ML gold grows in a 2D island fashion, whereas for 1.4 ML coverage 3D islands were observed on top of the ridges.

Annealing of the gold covered facets led to drastic changes in the morphology of the surface. After the first annealing of the sample to a temperature around 870 K the gold clusters on top of the facets disappeared and instead of that the gold atoms fully wetted the two sided ridges. A second annealing to a temperature around 930 K altered the morphology totally. The surface structure changed from two sided ridges to "three sided pyramids", which were arranged along the direction of the original ridges. A careful analysis of the pyramids structure showed that the $(01\bar{1}0)$ facet of the original ridges was also one of the pyramids facets. Therefore we conclude that the pyramidal structure developes due to the appearance of two new facets instead of the $(11\bar{2}1)$ facet.

After another annealing of the sample to a temperature of approximately 970 K this pyramids disappeared again and a new surface structure consisting of two sided ridges emerged. These ridges, which were not well defined, were rotated by around 90° with respect to the direction of the oxygen induced ridges. This surface structure is referred to gold induced faceting on a planar Re $(12\bar{3}1)$ structure, since the same ridges structure was found on the planar $(12\bar{3}1)$ surface after dosing gold on it and annealing it.

Further annealing of the sample to higher temperatures did not show any evidence for new surface structures. Finally, after annealing above 1200 K, all surface structures were destroyed and gold desorbed from the surface.

This evolution of the morphology of the surface suggests that gold has the ability to induce new facets on the faceted rhenium surface. The fact that the $(01\bar{1}0)$ facet still exists in the pyramidal structure indicates that the new facets that appear to form the pyramidal structure emerge on the $(11\bar{2}1)$ facet side. Therefore it is believed that gold has also the capability to induce faceting on a planar Re $(11\bar{2}1)$ surface.

The morphological evolution of the surface structure due to annealing is generally the same for different coverages. But there is one distinct difference in this morphological change. It turned out that the development of the pyramidal structure depends on the gold coverage.

For a gold coverage of 0.4 ML it was found that one of the pyramids facet is underdeveloped. This leads to the conclusion that there is a minimum coverage that is required in order to fully develop the pyramidal structure. Since all of the pyramids facets seem to be fully developed and well defined for a coverage of 0.8 ML, the minimum gold coverage should be located between 0.4 ML and 0.8 ML.

For a gold coverage of 1.4 ML the pyramidal structure was found to be fully developed. But their shape was not as well defined and the long range order of the pyramids structure was lost. This beginning destruction of the pyramids is attributed to the fact that the necessary annealing temperature in order to fully develop the pyramidal structure

increases with the coverage. For a coverage of 1.4 ML the required temperature to develop the pyramidal structure is higher than the temperature at which the destruction of the oxygen induced facets starts. Therefore the pyramids are not as well developed and look a little bit destroyed for a coverage of 1.4 ML.

In order to better understand the pyramidal structure, more detailed studies were performed on it. By means of LEED and tilt angle calculations the orientations of the pyramidal facets were determinated as $(12\bar{3}2)$, $(01\bar{1}0)$ and $(11\bar{2}0)$.

Also information about the atomic structure of the facets was obtained by analyzing atomically resolved STM images. The $(12\bar{3}2)$ facet shows a quasi-honeycomb atomic structure. Since this structure does not agree with the hcp $(12\bar{3}2)$ atomic structure it is suspected that this facet is covered by a gold overlayer. The $(01\bar{1}0)$ facet shows a atomic structure that matches the structure for the hcp $(01\bar{1}0)$ orientation. Therefore it is believed that this facet is not covered by gold atoms. It was not possible to obtain atomically resolved STM images for the $(11\bar{2}0)$ facet. Thus no conclusions about the atomic structure of this facet can be drawn.

Furthermore a correlation between the pyramids size and the size of the oxygen induced ridges was found. The size of the pyramids increases with the size of the ridges. Hence the size control of the oxygen induced ridges is well understood, this fact can be used to control the size of the pyramids.

Depositing gold on a planar Re $(12\bar{3}1)$ substrate followed by annealing of the sample to a temperature of approximately 970 K led to the development of two sided ridges on top of the surface. This morphological change suggests that gold also has the ability to induce faceting on a planar Re $(12\bar{3}1)$ surface. The direction of the gold induced ridges appeared to be rotated by around 90° with respect to the direction of the oxygen induced facets. By considering this rotation and the analysis of STM images of the ridges

structure the most likely orientation for the ridges was found to be $(12\bar{3}0)$ and $(12\bar{3}2)$.

The morphological changes observed on both the oxygen induced faceted and the planar rhenium surface are attributed to adsorbate induced faceting with gold as adsorbate. Adsorbate induced faceting is believed to be thermodynamically driven by the anisotropy of surface free energy. For clean metal surfaces the anisotropy of surface free energy is always too small to cause faceting. But a thin overlayer film can increases the anisotropy of surface free energy and thereby make surface facets energetic favorable.

Within this thesis it was found that the gold covered oxygen induced two sided ridges underwent a morphological evolution after annealing. Thereby new facets developed instead of the $(11\bar{2}1)$ facet, whereas the $(01\bar{1}0)$ facet remained unchanged until all facets were destroyed. This behavior can be understood considering surface free energies. $(11\bar{2}1)$ is an atomically rough surface with four atomic layer exposed. Atomically rough surfaces generally have a high surface free energy relatively to more close-packed surfaces. Therefore is is very likely that faceting is induced on the $(11\bar{2}1)$ facet. By contrast, $(01\bar{1}0)$ is a close-packed surface with low surface free energy; it is very unlikely to cause faceting on it. Also, Re $(12\bar{3}1)$ is an atomically rough surface with six atomic layers exposed. Consequently it is plausible that faceting could be induced on the planar surface, too.

In summary, the combination of gold adatoms dosed on a Re $(12\bar{3}1)$ substrate turned out to be a very rich combination. Many interesting and unexpected results were obtained on it and new physical properties were discovered. The discovery of gold induced faceting on the Re $(12\bar{3}1)$ surface underlines the diversity of metal on metal systems one more time. Previous studies on the same faceted Re $(12\bar{3}1)$ crystal with cobalt adatoms led to an entirely different result, the preferential nucleation of cobalt nanoclusters on the faceted rhenium surface [38]. But also gold induced faceting on transition metals is

nothing new. It was observed before for many different substrate materials, for example on a W (111) crystal [39].

In order to expand the understanding of the interaction between gold adatoms and the rhenium substrate there are a lot more experiments that can be performed. A more detailed study about the effect of gold on the planar Re $(12\bar{3}1)$ substrate would be desirable, for example. Also experiments on a planar Re $(11\bar{2}1)$ crystal would be very interesting, since the results reported in this work suggest that gold also can induce faceting on this surface orientation. On top of additional experiments it would be nice to perform density functional theory calculations connected to the gold/rhenium system. By adding a theoretical component a more complete understanding of the gold/rhenium system would be possible.

A full understanding of the Au/Re system finally might lead to a couple of interesting applications. So there are many applications in the field of catalysts imaginable, as both gold and rhenium are very popular metals in recent catalysts. [40], [41]

But whatever the applications eventually might be, this work should definitely motivate more studies with Au/Re systems, as it is a really interesting and "facetinating" system.

Appendix A

Preparation of tungsten tips for STM

All STM images shown in chapter 6 were obtained with home-made STM tips. The tips were produced by etching a tungsten wire in a sodium hydroxide solution. The used tungsten wire had a purity of 99.95 % and a diameter of 0.25 mm. The solution was manufactured by dissolving NaOH pellets in distilled water. The NaOH concentration of the used solution was about 2 mol/liter.

In order to fabricate a STM tip the tungsten wire is placed in the center of a platinum ring with an approximated diameter of 1 cm. Then a thin film of the etching solution is created on a platinum ring (Figure: A.1 a).

By applying an electrical potential between the platinum ring (cathode) and the tungsten wire (anode) the etching process starts. The potential which was used to produce tips was 5 V. It takes approximately half an hour to etch one STM tip completely. Etching is completed if the bottom part of the wire falls down from the ring (Figure: A.1 b). This is the part that will be used as STM tip. It is collected in a narrow plastic cylinder that is placed right below it. Then it is taken out of the cylinder and cleaned carefully with distilled water.

The quality of the manufactured tips was controlled with an optical microscope. But even if a tips seems to be sharp under an optical microscope it really might be blunt on a sub-micrometer scale. Therefore it is recommended to further examine the homemade tips with scanning electron microscopy before putting them in the STM.

A tip manufacturing-technique similar to the one above is described in [42].

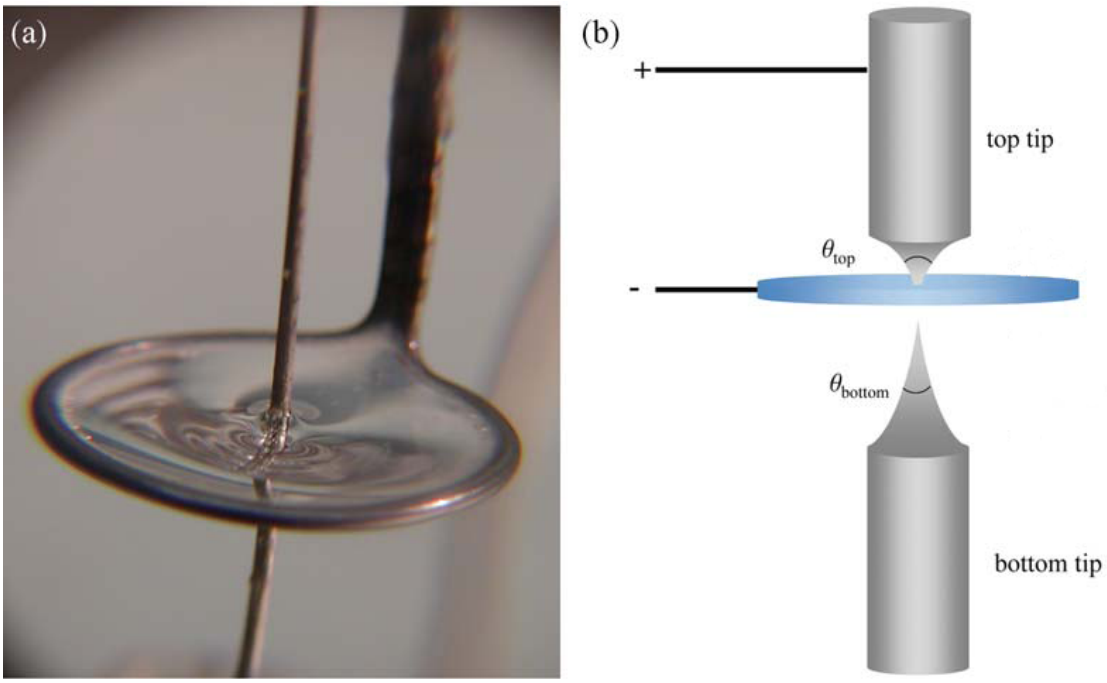

Figure A.1: a) The platinum ring covered with etching solution and the tungsten wire in the center. b) Schematics of etching a STM tip. [30]

Appendix B

List of abbreviations and acronyms

Å	Ångström, unit of length ; 1 Å = 1.0×10^{-10} m
AES	Auger electron spectroscopy
erg	Unit of energy ; 1 erg = 1.0×10^{-7} Joule
ECS	Equilibrium crystal shape
hcp	hexagonal close-packed
fcc	face-centered cubic
LEED	Low energy electron diffraction
ML	Monolayer
Torr	Unit of pressure ; 1 Torr = 133,322 Pascal
STM	Scanning tunneling microscopy or scanning tunneling microscope
TSP	Titanium sublimation pump
UHV	Ultra high vacuum
x-slope	Processing mode for STM images; thereby the derivative of the height in x-direction is taken

References

[1] *http://www.census.gov/ipc/www/idb/worldpopinfo.html*

[2] *http://news.bbc.co.uk/sport2/hi/front_page/6934955.stm*

[3] G. A. Somorjai, Y.G. Borodko ; Catal. Lett., 76, 2001, 1

[4] I. Chorkendorff, J. W. Niemantsverdriet ; *Concepts of modern catalysis and kinetics* ; Wiley-VCH Verlag, 2003

[5] Claude R. Henry ; Surface Science Reports, 31, 1998, 231

[6] *http://www.webelements.com/rhenium*

[7] G. C. Bond, C. Louis, D. T. Thompson ; *Catalysis by gold* ; Imperial College Press, 2006

[8] D. E. Gray ; *American Institute of Physics Handbook* ; Mcgraw-Hill, 3rd edition, 1972

[9] *www.mtu.de/de/technologies/engineering_news/zukuenftige_anforderungen_an_hochtemperaturwerkstoffe.pdf*

[10] *http://www.americanelements.com/ingot.jpg*

[11] R. W. Vook, M. A. Otooni ; J. Appl. Phys., 39, 1968, 2471

[12] *http://www.webelements.com/gold/*

[13] The Bible, Gospel of Matthew (2:1-12)

[14] *http://news.bbc.co.uk/2/hi/business/7186570.stm*

[15] *http://www.greece-athens.com/pages_images/14.jpg*

[16] Steven P. Nolan ; Nature, 445, 2007, 496

[17] Masatake Haruta ; Catalysis Today, 36, 1997, 153

[18] Zangwill A. ; *Physics at surfaces* ; Cambridge University Press, 1988

[19] Charles T. Campbell ; Surface Science Report, 27 , 1997, 1

[20] T. E. Madey ; *Nucleation and growth of thin films; epitaxial growth* ; Surface Science Lecture Notes

[21] G. Ehrlich, F. G. Hudda ; J. Chem. Phys., 44, 1966, 1039

[22] R. L. Schwoebel ; J. Appl. Phys., 40 ,1969, 614

[23] C.T. Campbell, A. Ludviksson ; J. Vac. Sci. Technol., A 12, 1994, 64

[24] Hao Wang, Wenhua Chen, T. E. Madey ; Physical Review B , 74, 2006, 205426

[25] I. Ermanoski ; *Nanoscale properties of planar and faceted Ir(210)* ; Ph.D. Thesis, Rutgers University, 2005

[26] A. Roth ; *Vacuum technology, second revised edition* ; North-Holland Physics Publishing (1986)

[27] D. Meschede, C. Gerthsen ; *Physik* ; Springer-Verlag, 2004

[28] P. M. Marcus, F.Jona ; *Determination of surface structure by LEED* ; Plenum Press, 1984

[29] H. Wang, Wenhua Cheng, Ally S. Y. Chan, T. E. Madey ; *Absorbate induced faceting of atomically rough Re surfaces: Re(*$12\bar{3}1$*), Re(*$11\bar{2}1$*)* ; American vacuum society, 53th international symposium, Poster presentation

[30] Elena Longinova ; *Two topics in surface science: Morphological changes of NiAl (111) induced by oxygen; Secondary electron yield studies of Ru and* $Ti0_2$ *surfaces related to extreme ultraviolet lithography* ; Ph.D Thesis, Rutgers University, 2008

[31] D. P. Woodruff, T. A. Delchar ; *Modern techniques of surface science* ; Cambridge University Press, 1988

[32] L. E. Davis, N. C. MacDonald, P. W. Palmberg, G. E. Riach, R. E. Weber, *Handbook of Auger electron spectroscopy* ; Physical Electronic Industries, 1976

[33] *http://www.nobelprize.org/nobel_prizes/physics/laureates/1986/index.html*

[34] N. John DiNardo ; *Nanoscale Characterization of Surfaces and Interfaces* ; VCH Verlagsgesellschaft, 1994

[35] K. W. Kolasinski ; *Surface science foundations of catalysis and nanoscience* ; John Wileys & Son, 2002

[36] C. Julian Chen ; *Introduction to Scanning Tunneling Microscopy* ; Oxford University Press, 1993

[37] Richard E. Honig, Dean A. Kramer ; RCA Review, 30, 2, 1969, 285

[38] M. Reyhan, H. Wang, T. E. Madey ; *Preferential nucleation of metallic clusters on a nanotemplate* ; Catal. Lett., 2008, accepted for publication

[39] K.J Song, C.Z. Dong, T. E. Madey ; *Faceting induced by ultrathin metal films: Pt and Au on W (*111*)* ; Springer series in surface science , Vol. 24, The structure of surfaces 3, 1991

[40] K. Liu, S.C. Fung, T.C. Ho, D.S. Rumschitzki ; Journal of catalysis, 206, 2002, 188

[41] Charles T. Campbell ; Science, 306, 2004, 234

[42] John T. Yates Jr. ; *Experimental innovations in surface science* ; Springer-Verlag, 1997

Vita

Robert Christoph Wolfgang Baier

Date of Birth: 03/08/1984

Hammelburg, Germany

2007 - 2008 Rutgers, The State University of New Jersey ; New Brunswick, New Jersey, USA ; Study of Physics, Degree: M.Sc. in Physics

2004 - 2007 Julius-Maximilian-Universität Würzburg ; Würzburg, Germany ; Study of Physics, Degree: "Vordiplom"

2003 - 2004 Carl von Heß Krankenhaus Hammelburg ; Hammelburg, Germany ; Civil Service

1994 - 2003 Frobenius Gymnasium Hammelburg ; Hammelburg, Germany ; Grammar School, Degree: "Abitur"

1990 - 1994 Grundschule Wartmannsroth ; Wartmansroth, Germany ; Elementary School